

## X-ray Emission Signatures of Neutron Star Mergers

CONNERY J. CHEN <sup>1,2</sup>, YIHAN WANG <sup>1,2</sup> AND BING ZHANG <sup>1,2</sup>

<sup>1</sup>*Nevada Center for Astrophysics, University of Nevada, 4505 S. Maryland Pkwy., Las Vegas, NV 89154-4002, USA*

<sup>2</sup>*Department of Physics and Astronomy, University of Nevada, 4505 S. Maryland Pkwy., Las Vegas, NV 89154-4002, USA*

Submitted to ApJ

### ABSTRACT

Neutron star (NS) mergers, including both binary NS mergers and black hole - NS mergers, are multi-messenger sources detectable in both gravitational waves (GWs) and electromagnetic (EM) radiation. The expected EM emission signatures depend on the source’s progenitor, merger remnant, and observer’s line of sight (LoS). Widely discussed EM counterparts of NS mergers have been focused in the gamma-ray (in terms of short-duration gamma-ray bursts) and optical (in terms of kilonova) bands. In this paper, we show that X-ray emission carries unique post-merger signatures that are inaccessible in other EM bands and plays an important role in understanding the physics and geometry of these mergers. We consider several binary progenitor and central engine models and investigate X-ray emission signatures from the prompt phase immediately after the merger to the afterglow phase extending years later. For the prompt phase, we devise a general method for computing phenomenological X-ray light curves and spectra for structured jets viewed from any LoS, which can be applied to X-ray observations of NS mergers to constrain the geometry. The geometric constraints can in turn be used to model the afterglow and estimate a peak time and flux—to preemptively determine afterglow characteristics would be monumental for follow-up observation campaigns of future GW sources. Finally, we provide constraints on the time window for X-ray counterpart searches of NS mergers across a range of luminosity distances and detector sensitivities.

*Keywords:* gamma-ray burst: general – stars: magnetars – methods: numerical – X-rays: stars

### 1. INTRODUCTION

The first gravitational-wave (GW) detection was made in 2015 by the LIGO and Virgo collaborations (Abbott et al. 2016), validating Einstein’s theories from a century ago and ushering in the era of GW astronomy. Since then, over 200 events have been detected, with the detection rate increasing exponentially due to advancements in detector sensitivity and data analysis techniques. The first detection of a binary neutron star (BNS) merger in 2017 through both GW (Abbott et al. 2017a) and electromagnetic (EM) observations (Abbott et al. 2017b; Goldstein et al. 2017; Savchenko et al. 2017; Troja et al. 2017; Valenti et al. 2017; Covino et al. 2017; Hallinan et al. 2017; Zhang et al. 2018a) marked the dawn of observational multi-messenger astrophysics. The source is still exhibiting interesting X-ray characteristics a few years later, which lead to interesting tests to physical models (Troja et al. 2020; Hajela et al. 2022). This re-

mains the first and only multi-messenger detection of a BNS merger.

In general, a neutron star (NS) merger involves at least one NS in the merger system. These systems, including both NS-NS mergers (also called binary NS mergers or BNS mergers), and NS - black hole (BH) mergers, are ideal multi-messenger systems that generate both GW and EM signals. Leading up to a NS merger, the binary system loses orbital energy through GW radiation, causing binary separation to decrease. The final outcome and associated GW and EM signals depends on the initial parameters of the system and the NS EoS, which is poorly constrained (Lattimer 2021; Burgio et al. 2021). For BNS mergers, the radioactive decay of r-process elements synthesized in neutron-rich material ejected from the merger can power a luminous transient known as a kilonova (Li & Paczyński 1998; Kulkarni 2005; Metzger et al. 2010; Kasen et al. 2013). In the case of NS-BH mergers, if the black hole is not too massive and/or

is spinning rapidly, the NS, assuming a relatively stiff EoS, can be tidally disrupted outside the innermost stable circular orbit of the BH, leaving behind neutron-rich ejecta that may produce a kilonova. Otherwise, the NS will plunge directly into the BH without significant mass ejection, resulting in little or no EM counterpart. For both BNS mergers and NS-BH mergers with tidal disruption, relativistic jets can be launched along the axis normal to the merger orbital plane, which is observable as a gamma-ray burst (GRB). In the case of the BNS merger GW170817, a short GRB 170817A was detected (Goldstein et al. 2017; Savchenko et al. 2017; Zhang et al. 2018a).

GRBs are the most luminous transient in the universe marking the most violent explosions that invoke catastrophic events that launch highly relativistic jets (e.g. Zhang 2018). Phenomenologically, they are classified into two types based on duration (Kouveliotou et al. 1993): short GRBs (sGRBs) with durations less than 2 seconds and long GRBs (lGRBs) with durations greater than 2 seconds. Multi-wavelength, multi-messenger observations have shown that in general lGRBs are associated with core-collapse of massive stars, as evidenced by their association with Type Ic supernovae (Woosley & Bloom 2006), and that sGRBs are mostly associated from BNS mergers, as evidenced by the GW170817/GRB 170817A association (Abbott et al. 2017b). However, long-duration GRBs with no associated SNe (Della Valle et al. 2006; Fynbo et al. 2006; Gehrels et al. 2006; Gal-Yam et al. 2006; Yang et al. 2015) and short-duration GRBs likely with massive star origins (Antonelli et al. 2009; Levesque et al. 2010; Xin et al. 2011; Rossi et al. 2022) led Zhang (2006) and Zhang et al. (2007) propose that physical classifications do not always align with phenomenological classifications and that one should define GRBs based on their physical origins, i.e., Type I GRBs that originate from compact-object mergers, and Type II GRBs that are associated with the core-collapse of massive stars. The need of such a classification scheme is recently strengthened with the detection of two more long-duration GRBs associated with kilonovae (Rastinejad et al. 2022; Yang et al. 2022; Levan et al. 2024; Yang et al. 2024; Sun et al. 2025) and one short-duration GRB associated with a supernova (Ahumada et al. 2021; Rossi et al. 2022). Indeed, as discussed in Zhang (2025), besides progenitor, the duration of a GRB can be also defined by central engine, emitter, and even geometry. In this paper, we adopt the more general progenitor-based classification scheme and label NS merger-associated GRBs as Type I GRBs.

Traditionally, the EM counterparts of NS mergers is believed to be most efficiently searched in the gamma-ray (for short GRB emission) and optical (for kilonova emission) bands (Metzger & Berger 2012). The broadband afterglow emissions for both the GRB and kilonova are also expected. Zhang (2013) proposed that GW sources due to BNS mergers can be followed by bright long-duration X-ray emission if the merger product is a long-lived magnetar instead of black hole. Such an X-ray counterpart can be sGRB-less if the line of sight is off from the sGRB jet axis (see also Sun et al. (2017, 2019)). The consequence of such a massive magnetar engine would enhance the brightness of the kilonova (Yu et al. 2013) and the broadband afterglow Gao et al. (2013). Candidate sGRB-less X-ray transients that might be of a BNS merger origin have been reported (e.g. Xue et al. 2019; Bauer et al. 2017; Quirola-Vásquez et al. 2024; Ai & Zhang 2021), so are candidate kilonovae with a putative magnetar engine (e.g. Gao et al. 2015, 2017). It is essential to further multi-messenger observations for future BNS merger events to study their merger products and the observing geometry, and more detailed theoretical modeling is called for.

In view of the advance of the X-ray capability of studying fast X-ray transients brought by the Einstein Probe (Yuan et al. 2022) and SVOM (Wei et al. 2016) missions, in this work, we focus on the X-ray band and explore how X-ray emission signatures can vary between different binary progenitors, central engine remnants, and observer viewing angles. We develop a general method to model prompt X-ray emission from various NS mergers. We present general X-ray afterglow models that can be used to guide and estimate follow-up observations based on prompt X-ray observations. The goal of this work is to provide a comprehensive framework for modeling X-ray emissions from NS mergers across observational epochs.

In Section 2 we review the evolution of NS mergers starting from various progenitors, explore possible merger remnants, consider theoretical models for long-lived central engines, and examine how viewing geometry affects observational results. In Section 3 we outline observational characteristics of emission components relevant to NS mergers, including prompt, wind, and afterglow emissions. We introduce a method to model prompt X-rays and a spindown-powered X-ray wind (for the case of a long-lived magnetar central engine) for any LoS, and produce corresponding X-ray afterglow light curves. In Section 4 we present observational expectations of NS mergers from typical progenitors and their plausible central engine remnants viewed from any angle. We highlight how one can seamlessly adopt these

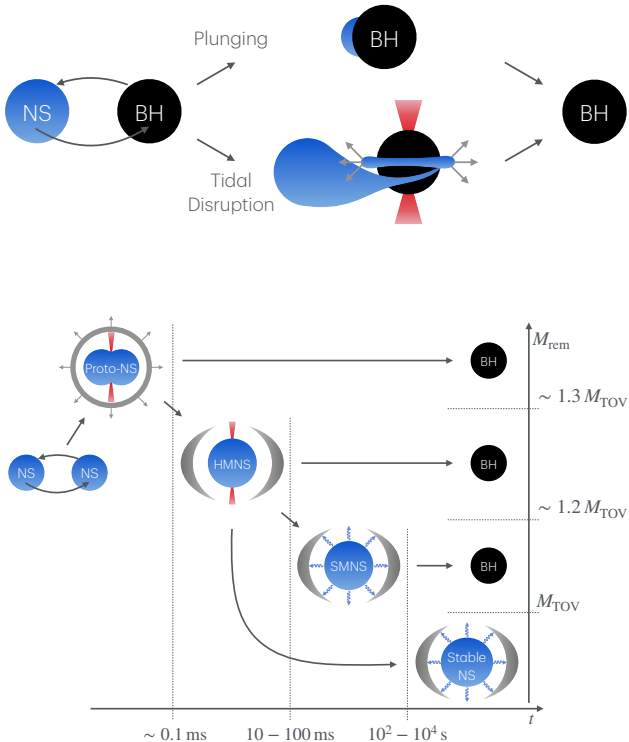


**Figure 1.** Central engine formation from a BH-NS merger (upper panel) and a BNS merger (lower panel).

results to observational campaigns in X-rays by providing a summarized workflow. We conclude our findings in Section 5.

## 2. CENTRAL ENGINE

Observations of GRB 170817A suggest that a jet dissipation activity initiates promptly at the time of or shortly after an NS merger (Abbott et al. 2017b,c; Goldstein et al. 2017; Savchenko et al. 2017). The source of internal energy dissipation processes that power the relativistic outflow and subsequent emission is the “central engine”. Typically, either a hyper-accreting black hole or a newly formed, rapidly rotating, and highly magnetized neutron star (magnetar) is proposed as the central engine.

The BH-NS merger product is always a black hole; thus, the formation of a hyper-accreting black hole central engine depends on whether the neutron star undergoes tidal disruption before plunging into the black hole (See upper panel of Fig. 1). The BNS merger product can either be a BH or long-lived magnetar central engine, depending on the remnant mass and equation of state (See bottom panel of Fig. 1, see also Gao et al. 2016; Margalit & Metzger 2019; Ai et al. 2020). In the following sub-sections we outline several possible central engines produced by NS mergers.

### 2.1. Black hole

For BH-NS mergers, if the BH is not sufficiently massive to directly swallow the NS, the NS can be tidally disrupted. In this scenario, the disrupted stellar material forms an accretion disk around the BH which can power jets (Janka et al. 1999; Rezzolla et al. 2011; Liu et al. 2017; Ruiz et al. 2021; Gottlieb et al. 2023a,b; Zhu et al. 2022) through the Blandford-Znajek mechanism (Blandford & Znajek 1977), and probably produce late-time X-ray flares (Perna et al. 2006; Proga & Zhang 2006).

For a non-spinning BH, the approximate criterion for tidal disruption of the NS is given by:

$$r_{\text{TD}} \sim \left( \frac{3M_{\bullet}}{M_{*}} \right)^{1/3} R > r_{\bullet} \sim \frac{2GM_{\bullet}}{c^2} \quad (1)$$

where  $r_{\text{TDE}}$  is the tidal disruption radius of the NS,  $r_{\bullet}$  is the event horizon of the BH,  $M_{\bullet}$  and  $M_{*}$  are the masses of the BH and NS, respectively, and  $R$  is the radius of the NS.

For BNS mergers, immediately before merger, some material with total mass  $M_{\text{ej}}$  will be dynamically ejected from the system and a remnant with total mass  $M_{\text{rem}}$  will remain. If  $M_{\text{rem}} \gtrsim 1.3 M_{\text{TOV}}$  (Ai et al. 2020; Metzger et al. 2010), a BH will be promptly formed within the dynamical timescale,

$$t_{\text{dyn}} = \left( \frac{R^3}{GM} \right)^{1/2} \approx 0.06 \left( \frac{R}{10\text{km}} \right)^{3/2} \left( \frac{M}{2M_{\odot}} \right)^{-1/2} \text{ms}. \quad (2)$$

### 2.2. Magnetar

While many models propose a hyper-accreting black hole as the central engine powering a GRB, Duncan & Thompson (1992) and Usov (1992) were among the first to propose that a newly formed, rapidly spinning, highly magnetized neutron star—a magnetar—could power a GRB by its enormous magnetic and spin energy reservoirs. Within the context of BNS mergers, a possible massive NS engine was first proposed by Dai et al. (2006) and Gao & Fan (2006) based on the argument that the mass of the merged remnant may be smaller than the maximum NS mass give a stiff enough NS EoS.

Notably, some sGRBs are followed by softer extended emission (Norris & Bonnell 2006) and a significant fraction of sGRBs exhibit “internal” X-ray plateaus—a distinct phase characterized by shallow to flat decay followed by a very steep temporal decay which cannot be interpreted within the framework of external shock models (Rowlinson et al. 2010, 2013; Lü et al. 2015). The long-duration Type I GRB 230307A displayed a distinct X-ray component that sustained when the  $\gamma$ -ray emission depleted, which is consistent with the spindown of

a magnetar engine (Sun et al. 2025). All these features are best interpreted with a spindown magnetar, probably with implosion (collapsing to a black hole) at the end (Zhang & Mészáros 2001; Metzger et al. 2008; Lü et al. 2015). A black hole engine (Kisaka & Ioka 2015; Lu & Quataert 2023; Hamidani et al. 2024) may interpret some of the less drastic plateaus but it is apparent that in order to account for the full Type I GRB data set as observed with Swift and other telescopes, a magnetar engine is demanded at least for some GRBs.

If a BNS merger remnant is not too massive to promptly collapse into a BH ( $M_{\text{rem}} \lesssim 1.3M_{\text{TOV}}$ ), it may evolve through short-lived phases (See bottom panel of Fig. 1).

### 2.2.1. Hypermassive Neutron Stars

If  $M_{\text{rem}} \sim (1.2 - 1.3)M_{\text{TOV}}$ , the remnant can withstand gravitational collapse by rapid differential rotation—the defining characteristic of an HMNS. Differential rotation is not sustained; as the NS spins, magnetic field lines are wound into strong toroidal components, launching Alfvén waves that carry angular momentum outward, reducing the degree of differential rotation. This process acts on a characteristic timescale (Shapiro 2000):

$$t_A = \frac{R}{v_A} \approx 1 \left( \frac{B_0}{10^{14} \text{ G}} \right)^{-1} \left( \frac{R}{10 \text{ km}} \right)^{-1/2} \left( \frac{M}{2M_\odot} \right)^{1/2} \text{ s.} \quad (3)$$

where  $v_A = B/(4\pi\rho^2)^{1/2}$  is the Alfvén speed. As magnetic braking reduces the degree of differential rotation, the HMNS loses centrifugal support. If the remnant mass still exceeds the maximum mass for a uniformly rotating NS (the supramassive limit), the remnant will promptly collapse to a black hole on the timescale of  $t_A$ .

It has been suggested that a Type I GRB jet may be launched during or shortly after the HMNS phase (e.g. Rosswog et al. 2003). Most & Quataert (2023) conducted numerical simulations showing that an HMNS can launch relativistic outflows that may explain precursor emission of Type I GRBs, or in some cases the Type I GRB itself.

### 2.2.2. Supramassive Neutron Stars

If  $M_{\text{rem}} \sim (1.0 - 1.2)M_{\text{TOV}}$ , then magnetic braking alone will not induce collapse. Even with no degree of differential rotation, a rapidly and rigidly rotating “supramassive neutron star” (SMNS) can withstand gravitational collapse until magnetic dipole or gravitational radiation removes sufficient rotation energy. The

Initial period	$P_0$	$10^{-3} \text{ s}$
Moment of Inertia	$I$	$10^{45}$
Polar magnetic field strength	$B_p$	$10^{15} \text{ G}$
Radius	$R$	$10^6 \text{ cm}$
Efficiency	$\eta_X$	$10^{-1}$
Remnant mass	$M_{\text{rem}}$	$2.7 M_\odot$
TOV mass limit	$M_{\text{TOV}}$	$2.25 M_\odot$

**Table 1.** Parameters for the model SMNS used in this work.

corresponding spindown luminosity is

$$L_{\text{sd}}(t) = \dot{E}_{\text{rot}}(t) = I\Omega\dot{\Omega} = -\frac{B_p^2 R^6 \Omega^4(t)}{6c^3} - \frac{32GI\epsilon^2 \Omega^6(t)}{5c^5} \quad (4)$$

where  $B_p$  is the polar magnetic field strength,  $R$  is the radius,  $\Omega$  is the angular velocity,  $I$  is the moment of inertia, and  $\epsilon$  is the ellipticity. The first term represents magnetic dipole spindown, and the second term represents GW spindown.

For typical SMNS parameters (Table 1), magnetic dipole radiation is far more efficient at dissipating rotational energy than gravitational wave radiation. Thus, the spindown luminosity follows

$$L_{\text{sd}}(t) \sim L_{\text{sd}}(0) \left( 1 + \frac{t}{t_{\text{sd}}} \right)^{-2} \quad (5)$$

where<sup>1</sup>

$$t_{\text{sd}} = \frac{E_{\text{rot}}}{\dot{E}_{\text{rot}}} = \frac{3c^3 I}{B_p^2 R^6 \Omega_0^2}. \quad (6)$$

For SMNSs, the collapsing time is usually close to the spindown timescale when the star is significantly spun down. The detailed collapsing time depends on the NS EoS,  $\Omega_0$  and  $B_p$ . In this paper, we follow the results of Ai et al. (2020) and adopt  $M_{\text{TOV}} = 2.25M_\odot$ ,  $M_{\text{SMNS}} = 1.2M_{\text{TOV}} = 2.7M_\odot$  as an example. For an SMNS with  $B_p \sim 10^{15} \text{ G}$ , the expected collapse time is  $t_c \sim t_{\text{sd}} \sim 300 \text{ s}$ .

### 2.2.3. Stable Neutron Star

If  $M_{\text{rem}} < M_{\text{TOV}}$ , the remnant will form a stable NS that can survive indefinitely. Shortly after merger, it will experience a brief phase of differential rotation before settling into uniform rotation. The stable NS is

<sup>1</sup> As in Gao et al. (2016), one can include both magnetic dipole and GW radiations and derive the spindown law directly from equation 4,

$$t = \frac{a}{2b^2} \ln \left[ \left( \frac{a\Omega_0^2 + b}{a\Omega^2 + b} \right) \frac{\Omega^2}{\Omega_0^2} \right] + \frac{\Omega_0^2 - \Omega^2}{2b\Omega_0^2\Omega^2}$$

where  $a = (32GI\epsilon^2)/(5c^5)$  and  $b = (B_p^2 R^6)/(6c^3 I)$ .

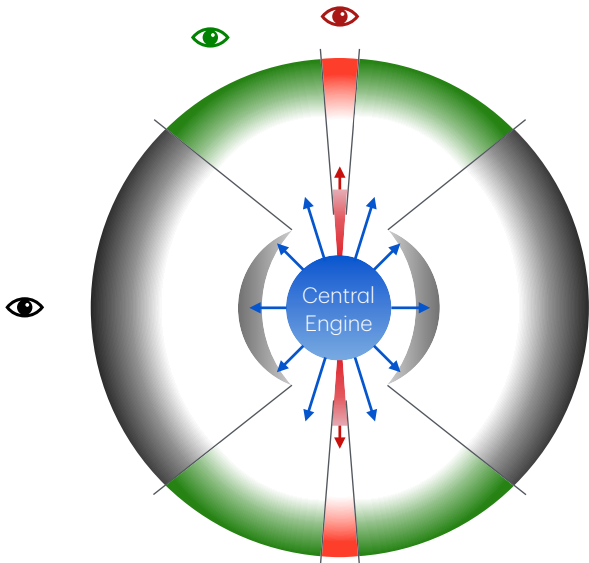


**Figure 2.** The geometric configuration of a NS merger system after the merger, which includes a jet zone (red), a free zone (green), and a trapped zone (black). In the jet zone, one sees the brightest region of emission from the jet core. In the free zone, one sees off-axis jet emission and can observe the central engine directly. In the trapped zone, relevant only when considering an opaque ejecta (i.e., a kilonova), one cannot observe the central engine directly but may still see off-axis emissions from the jet and central engine. Adapted from Sun et al. (2017).

governed by the same physical processes and emission mechanisms as an SMNS, except it does not rely on rotational energy to withstand gravitational collapse. The remnant may go on to power additional EM signatures, subject to the spin period and magnetic field strength, which could manifest as sustained emission, similar to radio pulsars, or as episodic bursts, as seen in soft gamma-ray repeaters and anomalous X-ray pulsars.

### 2.3. Viewing geometry

In BNS mergers and BH-NS mergers with successful tidal disruption of the neutron star, a fraction of disrupted material can be dynamically ejected. Due to the pre-merger orbital angular momentum, this ejecta is preferentially launched along the equatorial plane, while significantly less material is ejected along the polar (jet) axis. As a result, regardless of the central engine, the observed X-ray emission is strongly influenced by the viewing geometry (see Fig. 2).

If the observer’s line of sight is closely aligned with the jet axis—i.e., the viewing angle  $\theta_v$  is smaller than the jet opening angle  $\theta_c$  (the *Jet zone*)—bright gamma-ray and X-ray prompt emission from the jet can be observed directly. For viewing angles slightly outside the

jet ( $\theta_v > \theta_c$ ) but not obstructed by the dynamical ejecta (the *Free zone*), fainter prompt gamma-ray/X-ray emission may still be detected, depending on the angular structure of the jet and emission directly from the central engine. For magnetar engines with extended X-ray emission powered by a spindown wind, the emission can be viewed on-axis for both a jet-zone and a free-zone observer. However, if the observer’s line of sight lies within the *Trapped zone*, where the central engine is obscured by the dense equatorial ejecta, X-ray signals from the central engine would be significantly suppressed or entirely blocked.

The optical depth of the dynamical ejecta is given by

$$\begin{aligned} \tau &= \kappa \rho \Delta r \sim \kappa \frac{3M_{\text{ej}}}{4\pi(vt)^2} \\ &\approx 6 \times 10^7 \left( \frac{\kappa}{1 \text{ cm}^2 \text{ g}^{-1}} \right) \left( \frac{M}{10^{-2} M_{\odot}} \right) \\ &\quad \left( \frac{v}{0.1c} \right)^{-2} \left( \frac{t}{100 \text{ s}} \right)^{-2} \end{aligned} \quad (7)$$

where  $\rho$  is the average ejecta density and  $\Delta r \sim vt$  is the ejecta shell width. Initially, the ejecta is optical thick, however, as the ejecta expands, the optical depth decreases, and the *trapped zone* will eventually become transparent once  $\tau$  drops below unity. The corresponding transparency time is

$$\begin{aligned} t_{\text{thin}} &= \sqrt{\frac{3\kappa M_{\text{ej}}}{4\pi\beta v^2}} \\ &\approx 1.33 \times 10^5 \left( \frac{\kappa}{1 \text{ cm}^2 \text{ g}^{-1}} \right)^{1/2} \\ &\quad \left( \frac{M}{10^{-2} M_{\odot}} \right)^{1/2} \left( \frac{v}{0.1c} \right)^{-1/2} \text{ s} \end{aligned} \quad (8)$$

where  $\beta \approx 3$  is a parameter delineating the ejecta density profile (Metzger et al. 2010). Central engine activity occurring at  $t > t_{\text{thin}}$  can be directly observed even along lines of sight within the trapped zone. In contrast, any emission launched earlier than  $t_{\text{thin}}$  must diffuse through the ejecta, and will be delayed by the diffusion time:

$$t_{\text{diff}} = \frac{\Delta r}{c} \tau = \kappa \frac{3M_{\text{ej}}}{4\pi cvt}. \quad (9)$$

It is important to note that if the central engine is a magnetar, and its spin-down energy exceeds the kinetic energy of the dynamical ejecta, the ejecta can be accelerated. This acceleration reduces the optical depth of the ejecta more rapidly, potentially making  $t_{\text{thin}}$  much shorter and enabling earlier visibility of central engine emission (see, e.g., the “mergernova” scenario; Yu et al. 2013; Ai et al. 2022, 2025).

### 3. X-RAY EMISSIONS FROM NS MERGERS

#### 3.1. Prompt jet emission

For both BNS and NS-BH mergers, a relativistic jet is likely launched along the axis normal to the merger plane. The dissipation of the jet makes GRB prompt emission. The radiation mechanism of prompt emission is still not fully understood; leading candidates include synchrotron radiation from an optically thin region and quasi-thermal, Comptonized emission near the photosphere. Synchrotron self-Compton, external inverse Compton, and hadronic cascades have been also proposed to contribute to prompt emission.

Here, instead of involving uncertainties to model the prompt emission beginning from fundamental principles, we opt for a phenomenological approach. We model the temporal profile of a GRB pulse with the fast-rise-exponential-decay (FRED) function (Norris et al. 2005),

$$I(t) = \frac{A\lambda}{\exp(\tau_1/t + t/\tau_2)}, \quad t > 0, \quad (10)$$

where  $A$  is the normalization constant,  $\tau_1$  and  $\tau_2$  are the rise and decay timescales, and  $\lambda = \exp(2\mu)$ , where  $\mu = \sqrt{\tau_1/\tau_2}$ . Within this framework, the peak time is  $t_{\text{peak}} = \sqrt{\tau_1\tau_2}$ , the interval measured between two  $1/e$  amplitudes is  $\Delta t = \tau_2\sqrt{(1+4\mu)}$ , and the pulse asymmetry is defined by  $\tau_2/\Delta t$ .

We model the GRB spectrum with a Band function (Band et al. 1993),

$$N(E) = A \times \begin{cases} E^\alpha \exp\left(\frac{E(\beta - \alpha)}{E_b}\right), & \text{for } E < E_b \\ E_b^{\alpha - \beta} \exp(\beta - \alpha) E^\beta, & \text{for } E \geq E_b \end{cases} \quad (11)$$

where  $A$  is the normalization constant,  $E_b = (\alpha - \beta)[E_p/(2 + \alpha)]$  is the break energy, where  $E_p$  is the peak energy in the energy spectrum, and  $\alpha$  and  $\beta$  are the low- and high-energy photon indices.

The intrinsic gamma-ray energy profile of the jet is defined as

$$\epsilon_\gamma(\theta, \phi) \equiv \frac{dE_\gamma(\theta, \phi)}{d\Omega} = \frac{dE}{2\pi d\theta} \quad \left(\text{for } \frac{\partial \epsilon_\gamma}{\partial \phi} = 0\right), \quad (12)$$

where the final term assumes azimuthal symmetry, a common assumption in modeling structured jets. Under this assumption,  $\epsilon_\gamma(\theta, \phi)$  is a function of  $\theta$  only and hereafter we denote as  $\epsilon_\gamma(\theta)$ . In this work we adopt a Gaussian for the jet energy profile,

$$\epsilon_\gamma(\theta) = \begin{cases} \epsilon_{\gamma,0} \times \exp[-\theta^2/(2\theta_c^2)], & \theta \leq \theta_{\text{cut}} \\ 0, & \theta > \theta_{\text{cut}} \end{cases} \quad (13)$$

where  $\epsilon_{\gamma,0}$  is the peak energy per solid angle in gamma-rays and  $\theta_c$  is the characteristic Gaussian width of the

energy profile. A cutoff angle,  $\theta_{\text{cut}}$ , is applicable when modeling a source with an opaque ejecta (see Fig. 2).

Observationally, there is a correlation between Lorentz factor and isotropic energy of GRBs with  $\Gamma \propto E_{\text{iso}}^{1/4}$  (Liang et al. 2010; Ghirlanda et al. 2011). Assuming that different  $E_{\text{iso}}$  is essentially a result of observing a quasi-universal structured jet at different viewing angles (e.g. Zhang & Mészáros 2002), we adopt a Lorentz factor profile that follows a relation of  $\Gamma(\theta) \propto \epsilon_\gamma^{1/4}(\theta)$ , where variations in  $\Gamma$  and  $\epsilon_\gamma$  arise solely from differences in viewing angle. The Lorentz factor profile then writes

$$\Gamma(E_{\gamma, \text{iso}}) = \Gamma_0 (E_{\gamma, \text{iso}}/10^{52} \text{ erg s}^{-1})^{1/4} + 1, \quad (14)$$

where  $\Gamma_0$  is the normalization constant and the +1 term guarantees  $\Gamma > 1$ . Liang et al. (2010) and Ghirlanda et al. (2011) used observations of Type-II GRBs to find  $\Gamma_0 = 182$ . Although the corresponding value of  $\Gamma_0$  for Type-I GRBs remains uncertain, we adopt the same normalization as a phenomenological approximation. This choice is motivated by the lack of robust observational constraints for Type-I GRBs and the expectation that relativistic dynamics among GRBs remain similar.

Consider a structured GRB jet and two observers, one directly on the jet axis  $(\theta, \phi) = (0, 0)$  and one off the jet axis by an angle  $\theta_v$  with corresponding coordinates  $(\theta_0, \phi_0)$ . The on-axis observer sees the brightest portion of the jet, while the off-axis observer sees a much dimmer portion. Both observers can detect emission from surrounding regions of the jet, corrected for relativistic (Doppler) beaming effects.

The Doppler factor can generally be written as

$$\mathcal{D} \equiv \frac{1}{\Gamma(1 - \beta \cos \theta_v)}. \quad (15)$$

The on- and off-axis observers of a structured GRB jet will each calculate a particular Doppler factor,  $\mathcal{D}_{\text{on}}$  and  $\mathcal{D}_{\text{off}}$ , respectively. The ratio of Doppler factors is just  $\mathcal{R}_{\mathcal{D}} \equiv \mathcal{D}_{\text{off}}/\mathcal{D}_{\text{on}}$ . More generally, an observer with an arbitrary LoS  $(\theta_0, \phi_0)$ , will calculate a unique  $\mathcal{R}_{\mathcal{D}}$  for every other region at  $(\theta_i, \phi_j)$ ,

$$\mathcal{R}_{\mathcal{D}}(\theta_0, \phi_0, \theta_i, \phi_j) = \frac{\mathcal{D}(\theta_0, \phi_0)}{\mathcal{D}(\theta_i, \phi_j)} = \frac{1 - \beta}{1 - \beta \cos \theta_w} < 1, \quad (16)$$

where  $\theta_w$  is the angular distance between  $(\theta_0, \phi_0)$  and  $(\theta_i, \phi_j)$ .  $\mathcal{R}_{\mathcal{D}}$  relates observed jet properties between the on- and off-axis observers,

$$dt_{\text{off}} = \mathcal{R}_{\mathcal{D}}^{-1} dt_{\text{on}} \quad (17)$$

$$E_{\text{off}} = \mathcal{R}_{\mathcal{D}} E_{\text{on}} \quad (18)$$

$$d\Omega_{\text{off}} = \mathcal{R}_{\mathcal{D}}^{-2} d\Omega_{\text{on}}. \quad (19)$$

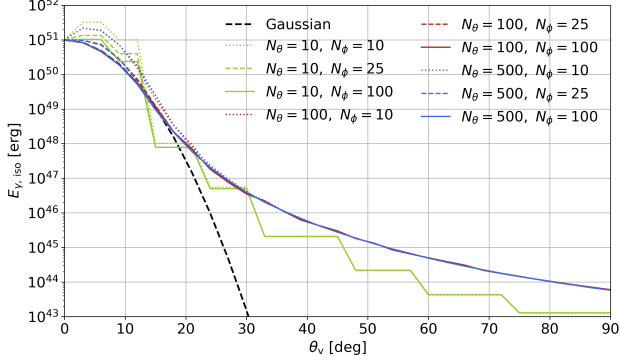


**Figure 3.** Observed isotropic-equivalent energy,  $E_{\gamma, \text{iso}} = 4\pi\bar{\epsilon}_{\gamma}$  (Eq. 20), for an observer at various  $\theta_v$ .

Numerically, we adopt a  $500 \times 100$  ( $\theta, \phi$ ) grid across  $2\pi$  steradians in spherical coordinates, with finer spacing near the jet axis at  $\theta = 0$ . This choice of resolution ensures an optimal balance between performance and accuracy in the following analyses (see Fig. 3). We define a Gaussian GRB jet with intrinsic  $\epsilon_{\gamma}$  (Eq. 13) and  $\Gamma$  (Eq. 14) profiles. In the Trapped zone,  $\epsilon_{\gamma}(\theta > \theta_{\text{cut}}) = 0$  and  $\Gamma(\theta > \theta_{\text{cut}}) = 1$ .

Consider again the observer viewing the jet from an arbitrary LoS with corresponding coordinates  $(\theta_0, \phi_0)$ . The *effective* energy per solid angle that the observer would detect from *all* emitting regions ( $\theta < \theta_{\text{cut}}$ ) is

$$\bar{\epsilon}_{\gamma}(\theta_0, \phi_0) = k_0 \frac{\sum_{i,j} \epsilon_{\gamma}(\theta_i, \phi_j) \mathcal{R}_{\mathcal{D}}^3 \Delta\Omega_{i,j}}{\sum_{i,j} \mathcal{R}_{\mathcal{D}}^2 \Delta\Omega_{i,j}}, \quad (20)$$

where  $k_0$  is the normalization factor, defined such that an on-axis observer detects an isotropic-equivalent energy in gamma-rays,  $4\pi\bar{\epsilon}_{\gamma}(0,0)$ , equal to a given (observed)  $E_{\gamma, \text{iso}}$ . Note that  $\bar{\epsilon}_{\gamma}(\theta_0, \phi_0)$  is composed of energy per solid angle along the LoS *and* Doppler-shifted energy per solid angle from surrounding patches—the observed energy per solid angle follows  $\bar{\epsilon}_{\gamma}(\theta_i, \phi_j) \propto \epsilon(\theta_i, \phi_j) \mathcal{R}_{\mathcal{D}}^3$ . Fig. 4 maps the observed energy per solid angle.

At each grid  $(\theta_i, \phi_j)$ , one can define an on-grid observer-frame spectrum,  $\partial N_{i,j}(E|E_p)/\partial\Omega = \mathcal{N}_{i,j}(E|E_p)$  (e.g., a Band function, Eq. 11). The notation  $(E|E_p)$  indicates that energy,  $E$ , is not directly Doppler-shifted but indirectly scaled through  $E_p$ , which is defined according to the empirical Amati relation,  $E_p \propto E_{\gamma, \text{iso}}^a$ , where  $E_{\gamma, \text{iso}} = 4\pi\bar{\epsilon}_{\gamma}(\theta_w)$ . Classically, for Type-II GRBs,  $a = 0.5$  (Amati et al. 2002). Later, it was found that Type I GRBs also have a similar correlation but with a track above the Type II branch (Zhang et al. 2009). A recent analysis (Minaev & Pozanenko 2020) gives  $a = 0.4$  for the short (Type I GRBs), which is adopted in this work. As we will demonstrate later,

assigning a Band function spectrum to each grid point is consistent with the Amati relation near  $\theta_v \sim \theta_c$ —the regime wherein the relation was originally established—and deviates at larger  $\theta_v$ . while still consistent with GRB 170817A within uncertainties of the Amati relation, which itself is an outlier to the classical Amati relation (see Fig. 7).

We adopt typical values of  $E_{p,0} \sim 1$  MeV,  $\alpha = -1$ , and  $\beta = -2.3$ . For each spectrum, the total gamma-ray energy per solid angle is

$$\epsilon_{\gamma, i,j} = A \int_{E_1}^{E_2} E \mathcal{N}_{i,j}(E|E_{p,0}) dE, \quad (21)$$

where  $E_1 = 10$  keV and  $E_2 = 1000$  keV are typical energy bounds for gamma-ray detectors (e.g., *Fermi-GBM*, *SWIFT-BAT* and *INTEGRAL*), and  $A$  is the normalization factor. The normalized spectra can be extended to X-rays and integrated to obtain the total X-ray energy per solid angle in each grid,  $\epsilon_{X, i,j} = A \int_{E_1}^{E_2} E \mathcal{N}_{i,j}(E|E_{p,0}) dE$ , where  $E_1 = 0.3$  keV and  $E_2 = 10$  keV.

Then, one can model an intrinsic gamma-ray (or X-ray) luminosity light curve per solid angle  $\mathcal{L}_{i,j} = \partial L_{i,j}/\partial\Omega$  at each grid (e.g., a FRED profile; Eq. 10) such that its time integral equals the total gamma-ray (or X-ray) energy per solid angle:

$$\epsilon_{\gamma, i,j} = \int_{t_1}^{t_2} \mathcal{L}_{\gamma, i,j}(t) dt, \quad (22)$$

$$\epsilon_{X, i,j} = \int_{t_1}^{t_2} \mathcal{L}_{X, i,j}(t) dt. \quad (23)$$

We choose the FRED model parameters,  $\tau_1 = 0.1$  s and  $\tau_2 = 0.4$  s (corresponding to  $\Delta t \approx 0.8$  s), so that the observed Doppler-broadened duration is consistent with GRB 170817A,  $T_{90, \text{GRB 170817A}} = (2 \pm 0.5)$  s (Goldstein et al. 2017). For  $E_{\gamma, \text{iso}, \text{GRB 170817A}} = 4.17^{+6.54}_{-0.99} \times 10^{46}$  erg (Zhang et al. 2018b), the isotropic-equivalent luminosity in gamma-rays is  $L_{\gamma, \text{iso}, \text{GRB 170817A}} = 2.09^{+3.27}_{-0.50} \times 10^{46}$  erg s $^{-1}$ .

For the observer at  $(\theta_0, \phi_0)$ , the spectra of other patches  $(\theta_i, \phi_j)$  appear Doppler-shifted,

$$\mathcal{N}_{i,j, \text{off}}(E) = \mathcal{N}_{i,j}(E|E_p(\theta_w)) * \mathcal{R}_{\mathcal{D}}^3(\theta_{\text{obs}}, \phi_{\text{obs}}, \theta_i, \phi_j). \quad (24)$$

One obtains the total observed spectrum per solid angle by combining the contributions from all emitting patches,

$$\mathcal{N}_{\text{tot}}(E) = \frac{\sum_{i,j} \mathcal{N}_{i,j, \text{off}}(E) \mathcal{R}_{\mathcal{D}}^3 \Delta\Omega_{i,j}}{\sum_{i,j} \mathcal{R}_{\mathcal{D}}^2 \Delta\Omega_{i,j}}. \quad (25)$$

For intrinsic spectra modeled as a Band function, the total observed spectrum still resembles a Band function, but with a smoother break, as shown in Fig. 5.

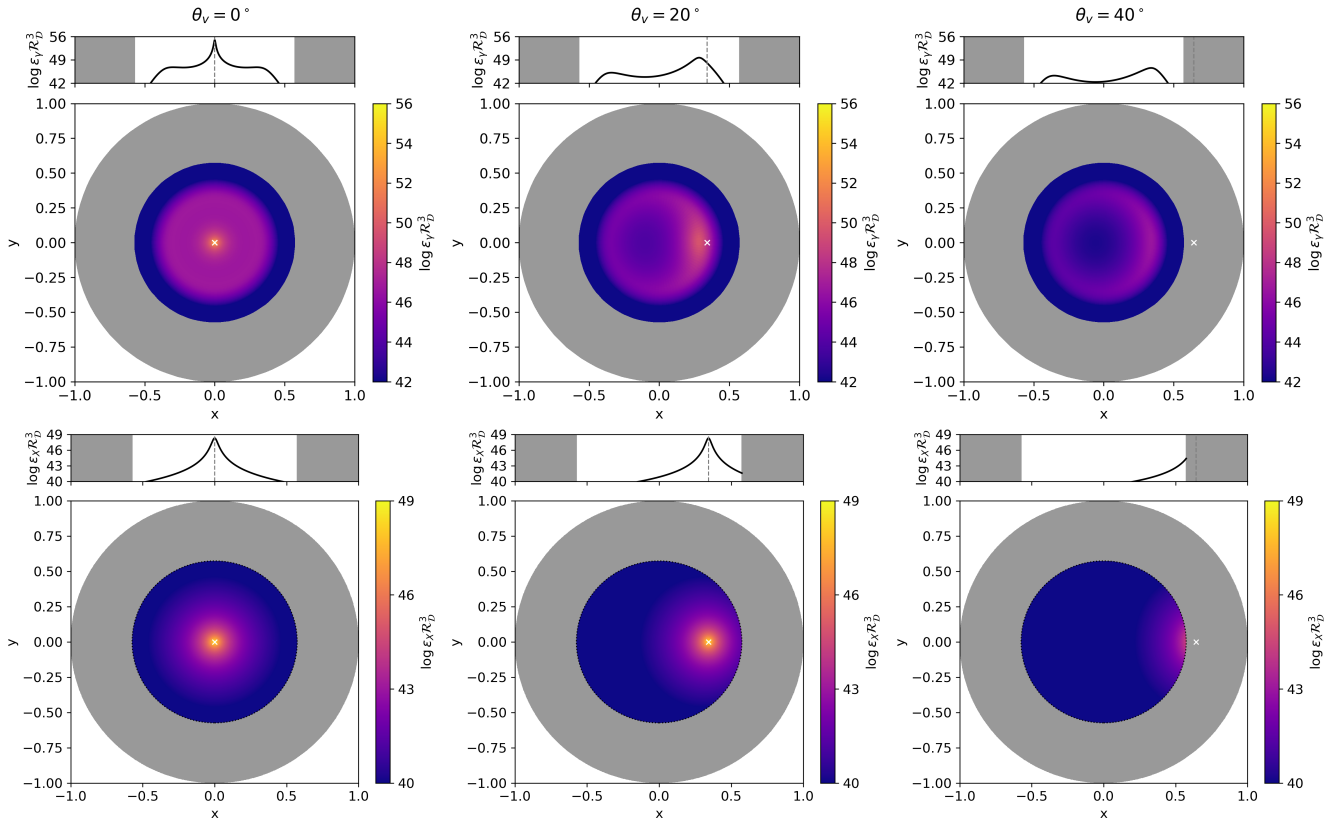


**Figure 4.** Maps of observed energy per solid angle,  $\epsilon \mathcal{R}_D^3$ , for a  $\theta_c = 5^\circ$  Gaussian GRB jet (top) and isotropic wind (bottom) for an observer at  $\theta_v = 0^\circ$  (left),  $\theta_v = 20^\circ$  (middle), and  $\theta_v = 40^\circ$  (right), with the observer's position marked by the white cross. The gray region indicates the Trapped zone, where  $\theta > \theta_{\text{cut}} = 35^\circ$ . The top panels show 1d diameter slices through  $\theta_v$ , indicated by the vertical dashed line.

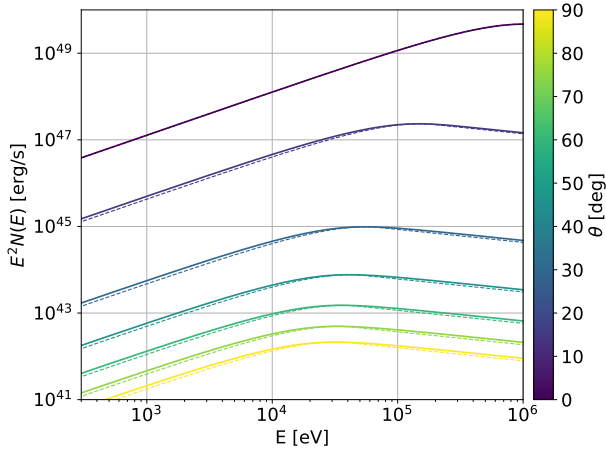


**Figure 5.** Total observed spectra (solid) compared to reference Band functions (dashed) with  $\alpha = -1$  and  $\beta = -2.3$  for various  $\theta_v$ . The reference Band functions are normalized such that the peaks are aligned to the observed spectra.

Similarly the duration and luminosity per solid angle of each patch are also Doppler-shifted,

$$\Delta t_{i,j,\text{off}} = \Delta t / \mathcal{R}_D(\theta_{\text{obs}}, \phi_{\text{obs}}, \theta_i, \phi_j) \quad (26)$$

$$\mathcal{L}_{i,j,\text{off}} = \mathcal{L}_{i,j} \mathcal{R}_D^2(\theta_{\text{obs}}, \phi_{\text{obs}}, \theta_i, \phi_j). \quad (27)$$

The total observed light curve per solid angle is then

$$\mathcal{L}_{\text{tot}} = \frac{\sum_{i,j} \mathcal{L}_{i,j,\text{off}} \mathcal{R}_D^4 \Delta \Omega_{i,j}}{\sum_{i,j} \mathcal{R}_D^2 \Delta \Omega_{i,j}}. \quad (28)$$

The total observed duration,  $\Delta t_{\text{tot}}$  is obtained by interpolating the individual durations  $\Delta t_{i,j,\text{off}}$  across the surface. The X-ray peak luminosity at different viewing angles is shown in Fig. 6.

Finally, by applying Eq. (21) to the total observed spectrum (Eq. 25), one obtains the total observed energy per solid angle,

$$\bar{\epsilon} = \int_{E_1}^{E_2} E \mathcal{N}_{\text{tot}}(E) dE, \quad (29)$$

which directly gives the observed isotropic-equivalent energy,  $E_{\text{iso}} = 4\pi \bar{\epsilon}$ , in any  $E_1 - E_2$  energy band. By

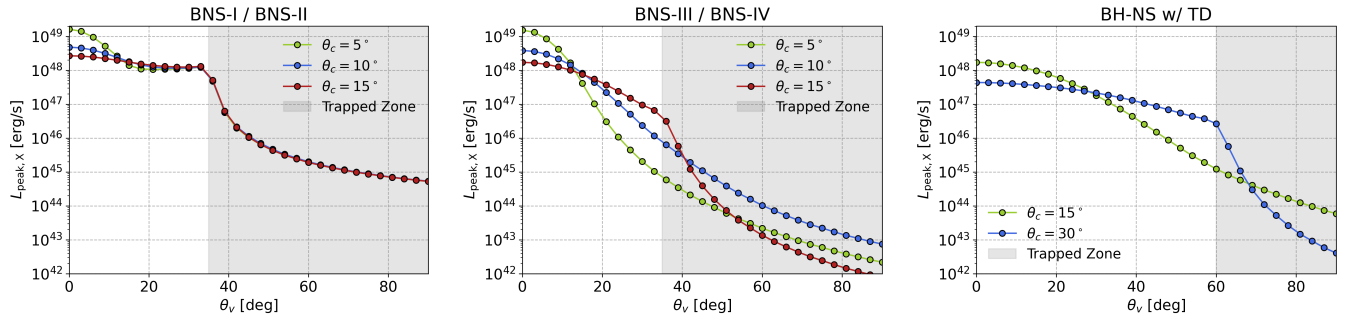


**Figure 6.** Prompt X-ray emission peak luminosity as a function of viewing angle. *Left panel* is for BNS mergers with a long-lived magnetar central engine. *Middle panel* is for BNS mergers without a long-lived magnetar central engine. *Right panel* is for BH-NS mergers. Total energy is fixed such that  $E_{\gamma, \text{iso}} = 10^{51}$  erg for  $\theta_c = 5^\circ$ .

the same token, the isotropic-equivalent luminosity is  $L_{\text{iso}} = 4\pi\mathcal{L}_{\text{tot}}$ .

As the observer moves off-axis from the core of a structured jet, the local emission along the line of sight ( $\theta_v$ ) diminishes significantly relative to the contribution from the bright jet core. For viewing angles  $\theta_v > \theta_c$ , most of the observed emission originates from an intermediate region between the LoS and jet axis—effectively the “brightest” visible region (see Fig.4). As a result, even when the intrinsic energy distribution is modeled with a Gaussian profile, the observed isotropic-equivalent energy  $E_{\text{iso}}(\theta_v)$  remains elevated at large viewing angles  $\theta_v \gg \theta_c$  (see Fig. 3).

In our model we assign each grid an intrinsic spectrum  $\mathcal{N}_{i,j}(E|E_p)$  with a peak energy  $E_p$  determined from the local isotropic-equivalent energy  $E_{\text{iso}}$  via the Amati relation. This setup ensures that emission near the jet axis (small  $\theta_v$ ) adheres to the classical Amati relation. However, for observers at large viewing angles ( $\theta_v \gg \theta_c$ ), the local emission is faint, and the observed spectrum is dominated instead by Doppler-shifted contributions from the brighter jet core. Since the jet core possesses both higher  $E_p$  and  $\bar{\epsilon}$ , the integrated spectrum is biased toward these brighter regions. Consequently, the observed spectrum primarily reflects the properties of the brightest contributing region near the jet core even though the total observed  $E_{\text{iso}}$  is significantly reduced due to Doppler effects. This leads to a substantially higher observed  $E_p$  than what would be predicted by the classical Amati relation, causing a noticeable deviation as illustrated in Fig. 7. This same deviation was observed in GRB 170817A, where the measured  $E_p$  was much higher than predicted by the Amati relation (Goldstein et al. 2017; Zhang et al. 2018a).

### 3.2. Wind emission

Specifically for BNS mergers with a long-lived magnetar central engine, there is a late emission component that originates from the nearly isotropic magnetar wind

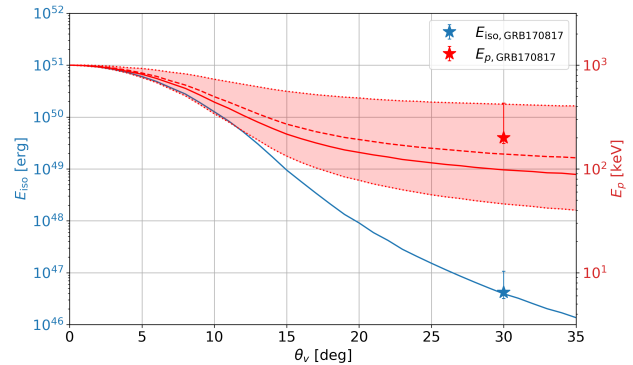


**Figure 7.** Observed isotropic-equivalent energy,  $E_{\text{iso}}$  (blue, left axis) and observed spectral peak energy  $E_p$  (red, right axis) as a function of viewing angle  $\theta_v$ . The red dashed line bounded by the red shaded region shows the Amati relation derived by Zhang et al. (2009),  $E_p \propto E_{\text{iso}}^{0.34 \pm 0.19}$ . The red solid line shows the Amati relation derived by Minaev & Pozanenko (2020) for Type I GRBs,  $E_p \propto E_{\text{iso}}^{0.4}$ , which is used in this work. Deviations at larger  $\theta_v$  occur because the observed spectrum is dominated by emission from the jet core, which maintains a higher intrinsic  $E_p$  despite strong Doppler deboosting of  $E_{\text{iso}}$ . GRB 170817A data obtained from (Zhang et al. 2018b).

due to the spindown of the magnetar. The X-ray luminosity of the wind is parameterized as

$$L_X(t) = \eta_X L_{\text{sd}}(t) \quad (30)$$

where  $\eta_X$  is the efficiency of converting spindown energy to X-ray luminosity. This factor is poorly known and model dependent (Rowlinson et al. 2014; Gao et al. 2016; Xiao & Dai 2019). In this work, we adopt  $\eta_X = 0.1$ . Using typical SMNS parameters (Table 1) in Eq. (4), we estimate the X-ray luminosity to be  $L_X \sim 10^{48}$  erg s $^{-1}$ . This corresponds quite well to typical X-ray plateau luminosities and provides a natural explanation for such emission (Lü et al. 2015). For a collapse time  $t_c = t_{\text{sd}} = 300$  s, the total wind energy is  $(3 \times 10^{51} \text{ erg}) \eta_{X,-1}^{-1}$ .

Numerically, we define an isotropic component with  $L_X = 10^{48} \text{ erg s}^{-1}$  and  $\Gamma_{\text{wind}} = 50$ . Unlike in Section 3.1, we do not define a spectral model for the X-ray wind. Instead we directly model the on-axis X-ray wind light curve using spindown luminosity (Eq. 5) and calculate  $\mathcal{L}_{X, i, j, \text{off}} = \mathcal{L}_{X, i, j} \mathcal{R}_{\mathcal{D}}$  for a given observer at  $(\theta_{\text{obs}}, \phi_{\text{obs}})$ . Then,  $\mathcal{L}_{X, \text{tot}} = \sum_{i, j} \mathcal{L}_{X, i, j, \text{off}} \mathcal{R}_{\mathcal{D}}^3 \Delta\Omega_{i, j} / \sum_{i, j} \mathcal{R}_{\mathcal{D}}^2 \Delta\Omega_{i, j}$ . Note that as long as  $(\theta_{\text{obs}}, \phi_{\text{obs}})$  is within the Free zone, the observer is “on axis” of the wind and  $L_X$  is unchanged. Once the observer is within the Trapped zone ( $\theta > \theta_{\text{cut}}$ ),  $\mathcal{R}_{\mathcal{D}} \neq 1$  and  $L_{X, \text{obs}}$  will be attenuated.

### 3.3. Afterglow

For both BNS and NS-BH mergers, the GRB jet interacts with the circumburst medium and decelerates, producing a pair of shocks: a relativistic forward shock propagating into the unshocked medium and a reverse shock propagating back into the unshocked jet (Mészáros & Rees 1997, 1999; Sari et al. 1998, 1999; Zhang et al. 2003). Both shocks accelerate electrons that radiate photons across a wide range of energies, from radio to gamma-ray and produce afterglow emission. The reverse shock is only relevant early on during and shortly after it passes through the jet, while the forward shock lasts much longer. The broadband emission produced by relativistic shocks from a GRB jet is termed the GRB afterglow emission. We use *VegasAfterglow* (Wang et al. 2025 in prep) to model X-ray afterglow light curves for a variety of jet geometries and observer’s LoS.

The more isotropic, non-relativistic kilonova ejecta would interact with the ambient medium to produce an ejecta afterglow. The emission is weak and usually buried beneath the bright GRB jet afterglow emission. It may, however, emerge when the jet enters the deep Newtonian phase at a much later time. The late time X-ray observation of GRB 170817A exhibited a flattening of the light curve—whether it is related to the emergence of the kilonova afterglow is inconclusive (Troja et al. 2020; Hajela et al. 2022). We model this component also using *VegasAfterglow* (Wang et al. 2025 in prep). We adopt isotropic dynamical ejecta with a total kinetic energy of  $\sim 10^{51}$  erg and an average initial velocity of  $\sim 0.2c$  (Villar et al. 2017; Cowperthwaite et al. 2017; Drout et al. 2017). For a magnetar central engine, energy injection into the dynamical ejecta has also been considered. All other parameters are consistent with those used for the jet afterglow, as listed in Table 2.

## 4. RESULTS

The evolution and fate of an NS binary and the associated EM signatures depend on the particular pair

of compact objects, the post-merger remnant, and the observer’s LoS to the system. For prompt and wind X-ray emission, we use the numerical model from Section 3 to produce prompt light curves for a variety of jet geometries and energetics, central engines, and viewing angles. The modeling parameters for prompt, wind and afterglow are summarized in Table 2.

### 4.1. BNS Mergers

A BNS merger can progress in several ways, based primarily on the remnant mass and angular velocity (upper panel of Fig. 1). In the following subsections, we adopt the following convention for labeling the evolutionary path based on ascending remnant mass:

1. BNS-I— $M_{\text{rem}} < M_{\text{TOV}}$ : The BNS merger will produce a differentially-rotating remnant (i.e., the HMNS “phase”). Once differential rotation becomes uniform, the remnant will spin down indefinitely as a stable NS.
2. BNS-II— $M_{\text{rem}} \sim (1.0 - 1.2) M_{\text{TOV}}$ : The BNS merger remnant will evolve through the HMNS phase and become a SMNS that will ultimately collapse into a BH once rotational energy is sufficiently dissipated by spindown.
3. BNS-III— $M_{\text{rem}} \sim (1.2 - 1.3) M_{\text{TOV}}$ : The BNS merger will evolve through the HMNS phase and will quickly collapse into a BH once differential rotation is sufficiently damped by magnetic braking.
4. BNS-IV— $M_{\text{rem}} \gtrsim 1.3 M_{\text{TOV}}$ : The BNS merger will promptly form a BH.

In all models of BNS mergers, we include an opaque ejecta beyond  $\theta_{\text{cut}} = 35^\circ$ , which is consistent with afterglow modeling of GRB 170817A (Troja et al. 2020). A physical interpretation assumes that the nearly isotropic ejecta is pierced by a jet, creating a narrow hole that is further widened by a magnetar wind preferentially directed along the jet axis (Wang et al. 2024) to  $\theta_{\text{cut}} = 35^\circ$ .

For each evolutionary path, we produce prompt and afterglow X-ray light curves following the method described in Section 3 (Figs 8 - 10). Observational data of GRB 170817A is over-plotted as a reference, serving as a qualitative check on the model behavior. We emphasize that this comparison is not intended as a fit, but rather as a rough benchmark to assess the general consistency of the BNS merger scenarios.

#### 4.1.1. BNS-I ( $BNS \rightarrow HMNS \rightarrow \text{stable NS}$ )

Physically, one would expect prompt and afterglow X-rays from the GRB jet and extended X-ray emission

**Table 2.** Model parameters for jet, magnetar wind and afterglow.

Model	$\epsilon(\theta)$	$\Gamma_0$	$E_{\gamma,\text{iso}}$ [erg]	$\theta_c$ [°]	$\theta_{\text{cut}}$ [°]	$L_{\text{sd},X}$ [erg/s]	$t_{\text{sd}}$ [s]	$E_{k,\text{iso}}$ [erg]	$n_{\text{ism}}$ [cm <sup>-3</sup> ]	$p$	$\epsilon_e$	$\epsilon_B$
BNS-I, BNS-II	Gaussian	100	$10^{51}$	5	35	$10^{48}$	300	$10^{52}$	0.05	2.15	$10^{-2}$	$10^{-3.7}$
BNS-III, BNS-IV	Gaussian	100	$10^{51}$	5	35	—	—	$10^{52}$	0.05	2.15	$10^{-2}$	$10^{-3.7}$
BH-NS w/ TD	Gaussian	60	$10^{50}$	15	60	—	—	$10^{51}$	0.05	2.15	$10^{-2}$	$10^{-3.7}$

from the wind of a long-lived remnant. The extended X-ray emission would not cease suddenly due to collapse but taper off with  $L_{\text{sd}} \propto t^{-2}$  (Eq. 5). The remnant is expected to be able to emit X-ray signals until it falls beneath the pulsar death line, and even then may still survive indefinitely.

Observationally, in X-rays, one would observe various emission signatures depending on the viewing angle,

- Jet zone: Bright prompt emission and decaying afterglow from the GRB jet. The extended wind emission becomes observable once the prompt emission sufficiently diminishes. See left panel of Fig. 8.
- Free zone: Faint prompt emission and rising afterglow from the GRB jet. The extended wind emission becomes observable once the prompt emission sufficiently diminishes—in some cases the prompt emission will never exceed the wind emission and only a plateau will be observed. See middle panel of Fig. 8.
- Trapped zone: Extremely faint prompt emission and dim late-time rising afterglow from the GRB jet. The extended wind emission becomes directly observable once the dynamical ejecta becomes optically thin. Doppler-shifted wind emission from the Free zone may be detectable. See right panel of Fig. 8.

#### 4.1.2. BNS-II ( $BNS \rightarrow HMNS \rightarrow SMNS \rightarrow BH$ )

Physically, one would expect prompt and afterglow X-rays from the GRB jet and extended X-ray emission from the wind of a long-lived remnant. The extended X-ray emission would cease suddenly at  $t_{\text{sd}}$  (Eq. 6), and only the X-ray afterglow would remain.

Observationally, in X-rays, one would observe various emission signatures depending on the viewing angle,

- Jet zone: Bright prompt emission and decaying afterglow from the GRB jet. The extended wind emission becomes observable once the prompt emission sufficiently diminishes, and will suddenly drop when the remnant collapses. See left panel of Fig. 9.

- Free zone: Faint prompt emission and rising afterglow from the GRB jet. The extended X-ray wind emission becomes observable once the prompt emission sufficiently diminishes—in some cases the prompt emission will never exceed the wind emission and only a plateau will be observed. The plateau will end abruptly when the remnant collapses. See middle panel of Fig. 9.

- Trapped zone: Extremely faint prompt emission and dim late-time rising afterglow from the GRB jet. If  $t_{\text{thin}} < t_c$ , the extended wind emission will become directly observable. See right panel of Fig. 9.

#### 4.1.3. BNS-III ( $BNS \rightarrow HMNS \rightarrow BH$ )

Physically, one would expect only prompt X-rays from the GRB jet. Observationally, in X-rays, one would observe various emission signatures depending on the viewing angle,

- Jet zone: Bright prompt emission and decaying afterglow from the GRB jet. See left panel of Fig. 10.
- Free zone: Faint prompt emission and rising afterglow from the GRB jet. See middle panel of Fig. 10.
- Trapped zone: Extremely faint prompt emission and dim late-time rising afterglow from the GRB jet. See right panel of Fig. 10.

#### 4.1.4. BNS-IV ( $BNS \rightarrow BH$ )

Remnants with masses much larger than the TOV mass limit will be unable to withstand collapse into a BH for an appreciable amount of time. A jet will still be launched and the associated light curve will likely resemble a BNS-III (Fig. 10)

#### 4.1.5. The case of GW 170817

The EM counterparts of GW 170817, including both prompt and afterglow emission, can be consistently interpreted within the framework presented here. However, since the earliest X-ray detections of GW 170817 were not until hours after the initial trigger, it remains unclear whether the NS merger of GW 170817 was a

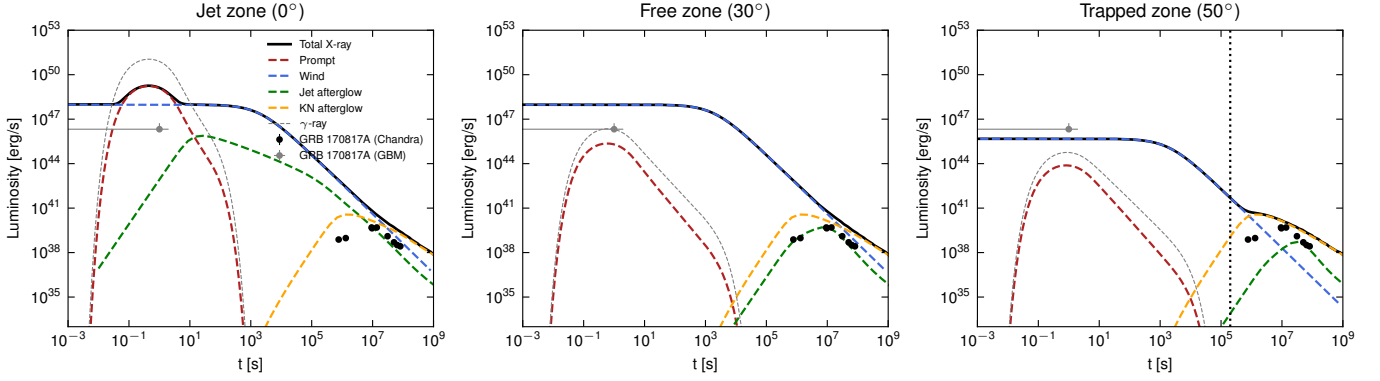


**Figure 8.** BNS-I model light curves composed of GRB prompt (red), magnetar wind (blue), GRB afterglow (green), and kilonova afterglow (yellow) emissions. Prompt emission is a fast-rise-exponential-decay model (Eq. 10) with peak luminosity corresponding to a Gaussian jet with  $\theta_c = 5^\circ$ ,  $E_{\gamma, \text{iso}} = 10^{52}$  erg, and  $t = 1$  s. Magnetar wind emission is calculated from spindown luminosity (Eq. 30) and assumed to be isotropic. GRB and kilonova afterglows are calculated using *VegasAfterglow*. We account for an opaque dynamical ejecta by imposing a cutoff,  $\theta_{\text{cut}} = 35^\circ$ , beyond which magnetar wind emission along  $\theta_v$  is blocked until the opacity time,  $t_{\text{thin}}$  (vertical dotted black line). GBM gamma-ray data was retrieved from Goldstein et al. (2017) and (Zhang et al. 2018b); Chandra X-ray data was retrieved from Troja et al. (2017); Troja et al. (2019a,b, 2020).

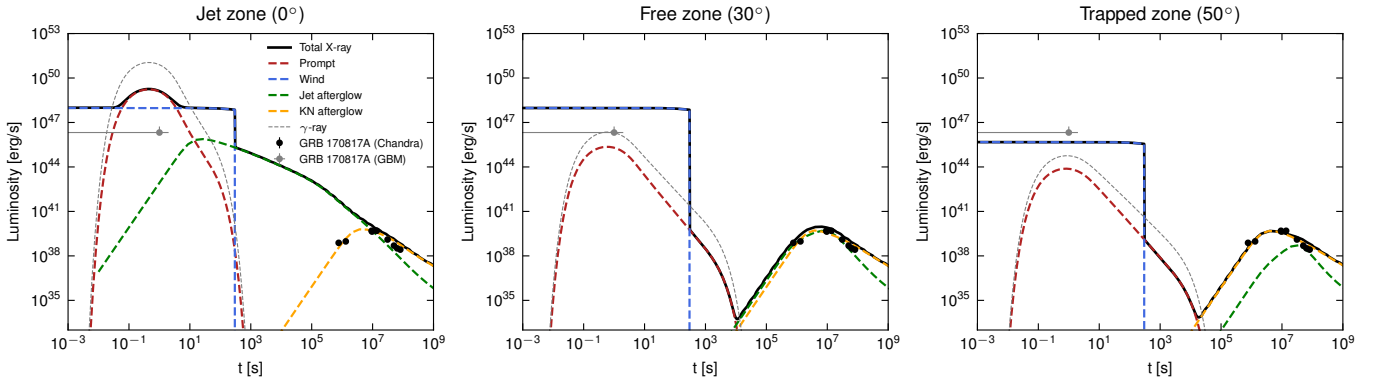


**Figure 9.** Same as Fig. 8 but for BNS-II.

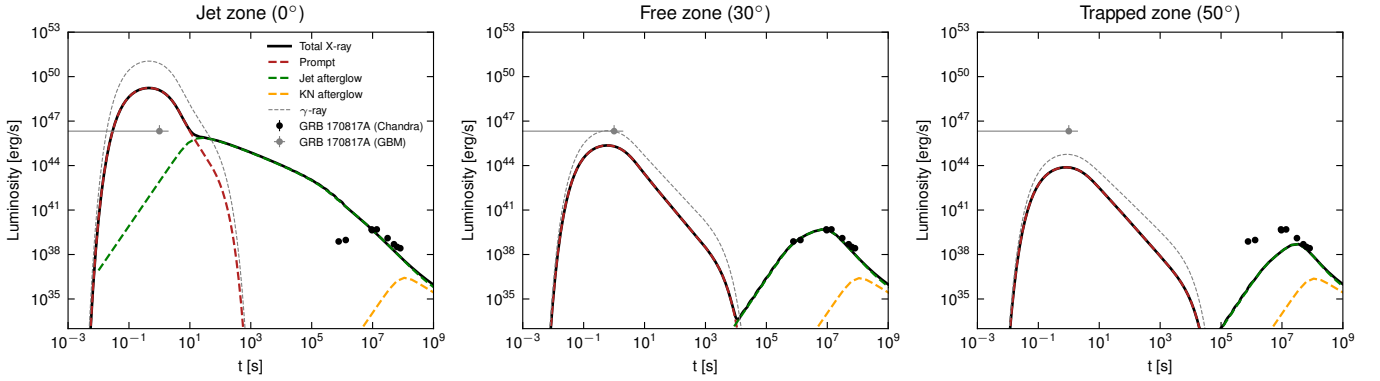


**Figure 10.** Same as Fig. 8 but for BNS-III and BNS-IV.

BNS-II or BNS-III/BNS-IV. Prompt X-ray detections of NS mergers by a wide-field X-ray detector such as EP-WXT can identify the presence of a long-lived central engine and distinguish between these scenarios.

#### 4.2. BH-NS Mergers

X-ray counterparts are expected only from BH-NS mergers that tidally disrupt the NS (BH-NS w/ TD). Physically, one would expect prompt and afterglow X-rays from a GRB jet. Compared to jets launched from BNS mergers, jets launched from BH-NS mergers w/ TD are likely less collimated (Bromberg et al. 2011; Duffell et al. 2015; Ruiz et al. 2018; Lazzati & Perna 2019). Additionally, the dynamical ejecta should be directed primarily in the equatorial direction (Kawaguchi et al. 2015, 2016). Therefore, we adopt  $\theta_c = 15^\circ$  and  $\theta_{\text{cut}} = 60^\circ$  for a BH-NS w/ TD jet and adjust  $E_{\text{iso}}$  such that the beaming-corrected energy  $E_\gamma = (1 - \cos \theta_c) E_{\text{iso}}$  remains constant. The BH-NS w/ TD jet, while less energetic than its BNS counterpart, has a shallower energy and Lorentz factor profile and larger cutoff angle, thus appearing brighter at large viewing angles.

Observationally, in X-rays, one would observe various emission signatures depending on the viewing angle,

- Jet zone: Bright prompt emission and decaying afterglow from the GRB jet. Fig. 11 (*left*).
- Free zone: Faint prompt emission and rising afterglow from GRB jet. Fig. 11 (*middle*).
- Trapped zone: Extremely faint prompt emission and dim late-time rising afterglow from the GRB jet. Fig. 11 (*right*).

#### 4.3. X-ray Counterpart Searches to Neutron Star Mergers

The search for EM counterparts of NS mergers detected by the LIGO-Virgo-KAGRA collaboration (LVK) is critical for advancing understanding of both the merger process and the Type I GRBs. The joint detection of GW170817 and GRB 170817A has opened a new era of multi-messenger astronomy, demonstrating the power of combining GW and EM observations.

With the ongoing improvement in sensitivity and detection volume of ground-based GW detectors, including future upgrades and next-generation observatories, we anticipate an increase in the number of detections of NS mergers with associated EM signatures. Therefore, establishing robust and timely follow-up strategies—particularly for the X-ray afterglows—is essential.

For any NS mergers with a potential EM counterpart, X-ray signals may arise from shock interactions, magnetar spin-down, fallback accretion, or relativistic jet

afterglows, and they typically evolve on timescales from hundreds of seconds to several years post-merger. Early detection of these signals can provide valuable insight into the nature of the remnant, energy dissipation mechanisms, and the surrounding environment.

Once candidates are localized, rapid follow-up observations using detectors like Swift/XRT (Gehrels et al. 2004) have historically proven invaluable for capturing the onset and evolution of X-ray afterglows. Its rapid response capability and sensitivity enable timely monitoring of transient sources.

The newest generation of wide-field X-ray telescopes, including the Einstein Probe (EP; Yuan et al. (2022)) and the Space-based multi-band astronomical Variable Objects Monitor (SVOM; Wei et al. (2016)), boasts rapid response and dedicated sensitivity in the soft X-rays. EP’s Wide-field X-ray Telescope (WXT), with its wide field-of-view and high sensitivity in the soft X-ray band (0.5–4 keV), is designed to promptly detect and localize soft X-ray transients across broad sky regions. Its on-board Follow-up X-ray Telescope (FXT), is a very sensitive X-ray instrument that allows deep follow-up observations in X-rays. SVOM offers complementary multi-wavelength capabilities through its diverse payload: the wide-field ECLAIR (4 – 150 keV) enables prompt detections, while the Microchannel X-ray Telescope (MXT; 0.2 – 10 keV) facilitates rapid X-ray follow-up. Additionally, SVOM is equipped with rapid slewing capability and is integrated with ground-based follow-up networks, enhancing its effectiveness in capturing transient events.

Motivated by these advancing observational capabilities and the need to prepare for future detections, here we present the intrinsic X-ray peak luminosity and time of prompt and afterglow emissions from NS mergers across all viewing angles. The results can be used jointly to provide a complete picture of X-ray emission signatures across wide observational epochs.

Fig. 6 shows the X-ray peak luminosity of prompt emission from NS mergers with EM counterparts observed at different viewing angles, assuming an isotropic-equivalent energy in gamma-rays  $E_{\text{iso}} = 10^{51}$  erg. For BNS mergers, the jet opening angle is typically narrow, with  $\theta_c \sim 5^\circ$ , as observed in GRB 170817A (Troja et al. 2017; Troja et al. 2019b, 2020), whereas for BH-NS mergers, the opening angle is likely larger,  $\theta_c \sim 15^\circ$  (Bromberg et al. 2011; Duffell et al. 2015; Ruiz et al. 2018; Lazzati & Perna 2019). Therefore, early prompt X-ray detections—or non-detections—with luminosity distance information inferred from LVK events could place meaningful constraints on the viewing angles of these mergers.

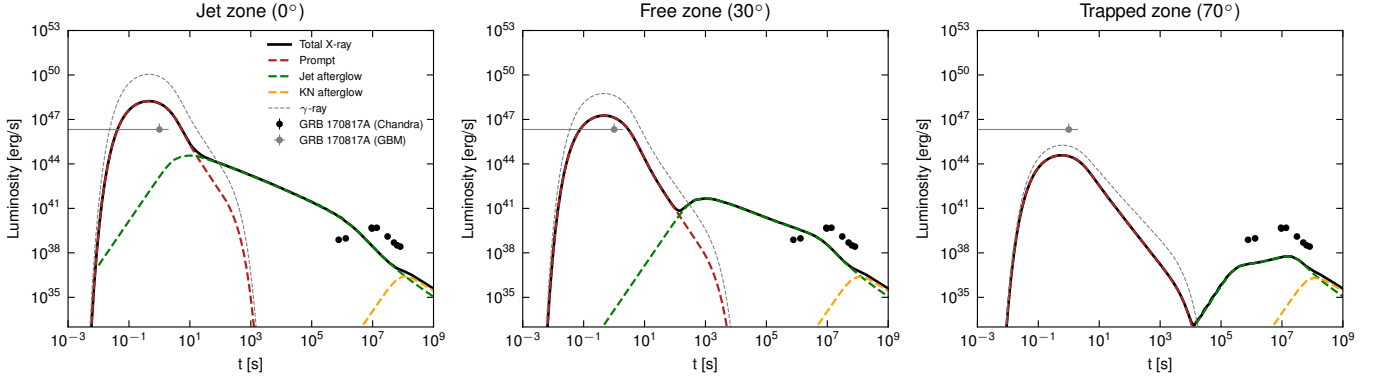


Figure 11. Same as Fig. 8 but for BH-NS w/ TD.

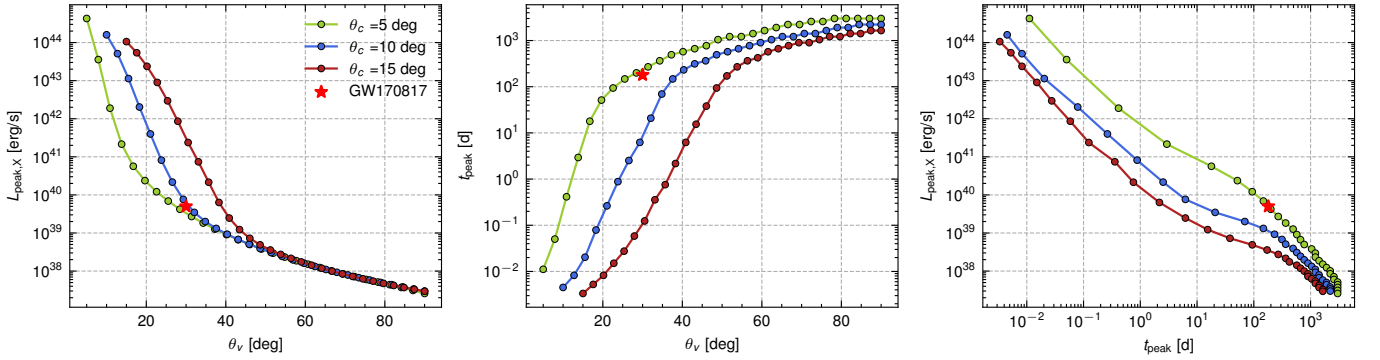


Figure 12. X-ray afterglow peak luminosity (*left panel*) and peak time (*middle panel*) as functions of viewing angle for a GW170817-like event. The *right panel* shows the correlation between peak luminosity and peak time. The beaming-corrected energy is fixed at  $10^{51}$  erg. X-ray data was retrieved from Troja et al. (2020).

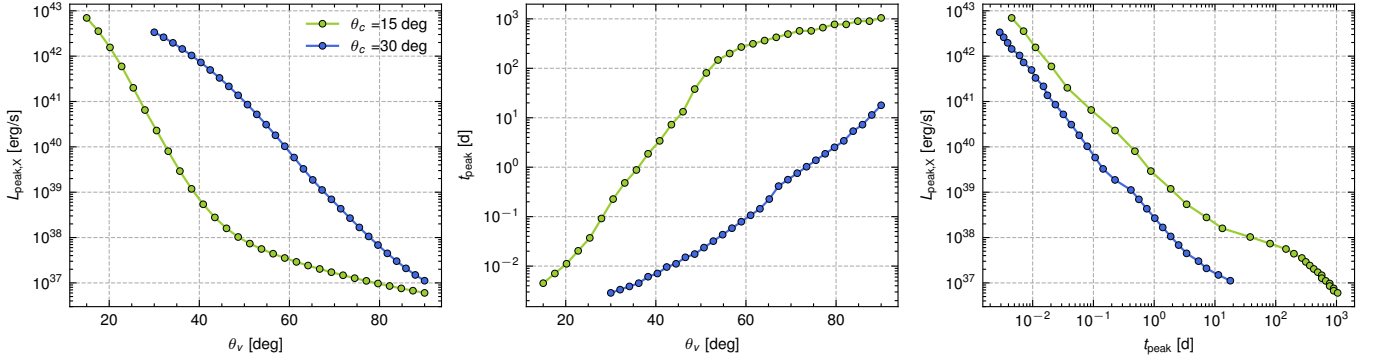


Figure 13. Same as Fig. 12, but for BH-NS w/ TD.

With this constraint, one may calculate the X-ray afterglow peak time and luminosity for reasonable Type I GRB parameters. Figure 12 shows the X-ray afterglow peak luminosity (*Left panel*) and peak time (*Middle panel*) as functions of the viewing angle  $\theta_v$ . The parameters are listed in Table 2. With the inferred luminosity distance from LVK, observers may estimate the detection horizon for X-ray counterparts of NS mergers

based on their detector's sensitivity and time since the GW trigger (Fig. 14).

Here we summarize the basic X-ray counterpart search workflow,

- **Detection:** An NS merger event is identified by either a GW signal detected by a GW observatory or a Type I GRB detected by a gamma-ray detector.

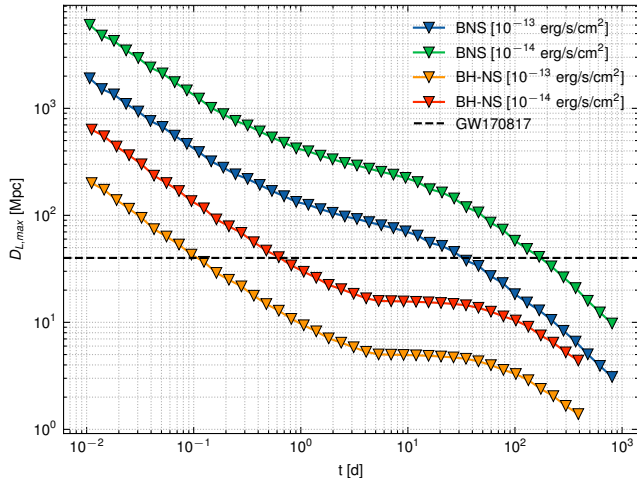


**Figure 14.** Detection horizon for X-ray (0.3-10 keV) afterglows from BNS/BH-NS mergers as a function of time, for given detector sensitivities. The model parameters are listed in Tab. 2.

- **Prompt X-ray Analysis:** Data from X-ray detectors that were covering the localized region during the trigger time should be examined for coincident events. If no events are found, upper limits can help constrain the prompt X-ray emission.
- **Viewing Angle Constraints:** Constraints can be obtained by X-ray detections and upper limits, using the model described in Section 3.1 and illustrated in Fig. 6. The inferred isotropic-equivalent luminosity,  $L_{\text{iso}} = E_{\text{iso}}/T_{90}$ , constrains the viewing angle  $\theta_v$ .
- **X-ray Afterglow Predictions:** With constraints on  $\theta_v$ , the X-ray afterglow characteristics can be estimated, e.g. the peak time and flux (Fig. 12).
- **Coordinated Follow-up:** X-ray follow-up observations can be planned based on the predicted afterglow properties. Using Figure 14, one can estimate the optimal time window for detecting an X-ray counterpart of an NS merger with known luminosity distance, given one’s detector sensitivity. It suggests that prompt follow-up observations are very important. In case of non-detection at a certain epoch, one can estimate the luminosity distance horizon beyond which continued follow-up is no longer necessary.

Additional detections of NS mergers with X-ray counterparts will be a major success of multi-messenger astronomy, and rapid follow-up observations play a crucial role in enabling such discoveries. According

to Figure 14, if EP-FXT (with sensitivity of about  $10^{-14}$  erg/s/cm<sup>2</sup>) does not detect an X-ray counterpart of a BH-NS merger within one day, then follow-up observations are no longer needed if the source is further than  $\sim 50$  Mpc. For BNS mergers, EP-FXT follow-up observations after one day are no longer needed for sources beyond  $\sim 300$  Mpc. Overall, the time window for follow-up searches is shortest for distant BH-NS mergers and longest for nearby BNS mergers.

## 5. CONCLUSION

In this paper, we have systematically investigated the X-ray signatures associated with NS mergers, considering various progenitors and central engines. We have introduced a method for modeling prompt X-ray light curves and spectra for any jet profile and observer viewing angle.

Our analysis specifically explored four distinct BNS merger scenarios categorized by remnant mass and post-merger evolutionary pathways: stable neutron star formation (BNS-I), delayed black hole collapse following a supramassive neutron star phase (BNS-II), rapid black hole formation post-hypermassive neutron star phase (BNS-III), and immediate black hole formation (BNS-IV). Each scenario revealed characteristic X-ray emission patterns: notably, long-lived magnetar remnants (BNS-I and II) produce distinct, prolonged X-ray plateau phases powered by magnetar spin-down emissions, which significantly differentiate them from scenarios leading directly or rapidly to black hole formation.

Furthermore, we highlighted how viewing geometry dramatically influences observed X-ray signatures, classifying observation zones into jet-aligned (brightest emission), free (moderately dimmed emission), and trapped (strongly dimmed or delayed emission due to ejecta opacity) zones. Such geometrical considerations are useful for interpreting X-ray data from multi-messenger observations, especially in conjunction with gravitational wave detections.

Last, we proposed a basic workflow for identifying and characterizing X-ray counterparts of GW-detected NS mergers, emphasizing rapid and coordinated follow-up strategies utilizing X-ray observatories such as Einstein Probe, SVOM, and Swift. This proactive observational approach will enhance our ability to detect, characterize, and interpret the physical processes underlying NS mergers.

## CODE AVAILABILITY

The code used to compute prompt X-ray emission from a relativistic jet and a magnetar-powered wind (see Sections 3.1 and 3.2) is publicly available under the MIT

license on GitHub: [github.com/cjules0609/PromptX](https://github.com/cjules0609/PromptX). The code for modeling GRB afterglow emission (see Section 3.3 and Wang et al. 2025, in preparation) is publicly available under the MIT license on Github: [github.com/YihanWangAstro/VegasAfterglow](https://github.com/YihanWangAstro/VegasAfterglow).

Both repositories provide the complete source code, accompanying documentation, and example scripts, enabling other researchers to reproduce the results and apply these methods to their own analyses.

## ACKNOWLEDGEMENTS

The authors acknowledge NASA 80NSSC23M0104, NASA 80NSSC20M0043, the Nevada Center for Astrophysics, and a UNLV Top-Tier Doctoral Graduate Research Assistantship (TTDGRA) for support.

## REFERENCES

- Abbott, B. P., Abbott, R., Abbott, T. D., et al. 2016, *PhRvL*, 116, 061102, doi: [10.1103/PhysRevLett.116.061102](https://doi.org/10.1103/PhysRevLett.116.061102)
- . 2017a, *PhRvL*, 119, 161101, doi: [10.1103/PhysRevLett.119.161101](https://doi.org/10.1103/PhysRevLett.119.161101)
- . 2017b, *ApJL*, 848, L12, doi: [10.3847/2041-8213/aa91c9](https://doi.org/10.3847/2041-8213/aa91c9)
- . 2017c, *ApJL*, 848, L13, doi: [10.3847/2041-8213/aa920c](https://doi.org/10.3847/2041-8213/aa920c)
- Ahumada, T., Singer, L. P., Anand, S., et al. 2021, *Nature Astronomy*, 5, 917, doi: [10.1038/s41550-021-01428-7](https://doi.org/10.1038/s41550-021-01428-7)
- Ai, S., Gao, H., & Zhang, B. 2020, *ApJ*, 893, 146, doi: [10.3847/1538-4357/ab80bd](https://doi.org/10.3847/1538-4357/ab80bd)
- . 2025, *ApJ*, 978, 52, doi: [10.3847/1538-4357/ad93b4](https://doi.org/10.3847/1538-4357/ad93b4)
- Ai, S., & Zhang, B. 2021, *ApJL*, 915, L11, doi: [10.3847/2041-8213/ac097d](https://doi.org/10.3847/2041-8213/ac097d)
- Ai, S., Zhang, B., & Zhu, Z. 2022, *MNRAS*, 516, 2614, doi: [10.1093/mnras/stac2380](https://doi.org/10.1093/mnras/stac2380)
- Amati, L., Frontera, F., Tavani, M., et al. 2002, *A&A*, 390, 81, doi: [10.1051/0004-6361:20020722](https://doi.org/10.1051/0004-6361:20020722)
- Antonelli, L. A., D’Avanzo, P., Perna, R., et al. 2009, *A&A*, 507, L45, doi: [10.1051/0004-6361/200913062](https://doi.org/10.1051/0004-6361/200913062)
- Band, D., Matteson, J., Ford, L., et al. 1993, *ApJ*, 413, 281, doi: [10.1086/172995](https://doi.org/10.1086/172995)
- Bauer, F. E., Treister, E., Schawinski, K., et al. 2017, *MNRAS*, 467, 4841, doi: [10.1093/mnras/stx417](https://doi.org/10.1093/mnras/stx417)
- Blandford, R. D., & Znajek, R. L. 1977, *MNRAS*, 179, 433, doi: [10.1093/mnras/179.3.433](https://doi.org/10.1093/mnras/179.3.433)
- Bromberg, O., Nakar, E., Piran, T., & Sari, R. 2011, *ApJ*, 740, 100, doi: [10.1088/0004-637X/740/2/100](https://doi.org/10.1088/0004-637X/740/2/100)
- Burgio, G. F., Schulze, H. J., Vidaña, I., & Wei, J. B. 2021, *Progress in Particle and Nuclear Physics*, 120, 103879, doi: [10.1016/j.pnpnp.2021.103879](https://doi.org/10.1016/j.pnpnp.2021.103879)
- Covino, S., Wiersema, K., Fan, Y. Z., et al. 2017, *Nature Astronomy*, 1, 791, doi: [10.1038/s41550-017-0285-z](https://doi.org/10.1038/s41550-017-0285-z)
- Cowperthwaite, P. S., Berger, E., Villar, V. A., et al. 2017, *ApJL*, 848, L17, doi: [10.3847/2041-8213/aa8fc7](https://doi.org/10.3847/2041-8213/aa8fc7)
- Dai, Z. G., Wang, X. Y., Wu, X. F., & Zhang, B. 2006, *Science*, 311, 1127, doi: [10.1126/science.1123606](https://doi.org/10.1126/science.1123606)
- Della Valle, M., Chincarini, G., Panagia, N., et al. 2006, *Nature*, 444, 1050, doi: [10.1038/nature05374](https://doi.org/10.1038/nature05374)
- Drout, M. R., Piro, A. L., Shappee, B. J., et al. 2017, *Science*, 358, 1570, doi: [10.1126/science.aag0049](https://doi.org/10.1126/science.aag0049)
- Duffell, P. C., Quataert, E., & MacFadyen, A. I. 2015, *ApJ*, 813, 64, doi: [10.1088/0004-637X/813/1/64](https://doi.org/10.1088/0004-637X/813/1/64)
- Duncan, R. C., & Thompson, C. 1992, *ApJL*, 392, L9, doi: [10.1086/186413](https://doi.org/10.1086/186413)
- Fynbo, J. P. U., Watson, D., Thöne, C. C., et al. 2006, *Nature*, 444, 1047, doi: [10.1038/nature05375](https://doi.org/10.1038/nature05375)
- Gal-Yam, A., Fox, D. B., Price, P. A., et al. 2006, *Nature*, 444, 1053, doi: [10.1038/nature05373](https://doi.org/10.1038/nature05373)
- Gao, H., Ding, X., Wu, X.-F., Dai, Z.-G., & Zhang, B. 2015, *ApJ*, 807, 163, doi: [10.1088/0004-637X/807/2/163](https://doi.org/10.1088/0004-637X/807/2/163)
- Gao, H., Ding, X., Wu, X.-F., Zhang, B., & Dai, Z.-G. 2013, *ApJ*, 771, 86, doi: [10.1088/0004-637X/771/2/86](https://doi.org/10.1088/0004-637X/771/2/86)
- Gao, H., Zhang, B., & Lü, H.-J. 2016, *PhRvD*, 93, 044065, doi: [10.1103/PhysRevD.93.044065](https://doi.org/10.1103/PhysRevD.93.044065)
- Gao, H., Zhang, B., Lü, H.-J., & Li, Y. 2017, *ApJ*, 837, 50, doi: [10.3847/1538-4357/aa5be3](https://doi.org/10.3847/1538-4357/aa5be3)
- Gao, W.-H., & Fan, Y.-Z. 2006, *ChJA&A*, 6, 513, doi: [10.1088/1009-9271/6/5/01](https://doi.org/10.1088/1009-9271/6/5/01)
- Gehrels, N., Chincarini, G., Giommi, P., et al. 2004, *ApJ*, 611, 1005, doi: [10.1086/422091](https://doi.org/10.1086/422091)
- Gehrels, N., Norris, J. P., Barthelmy, S. D., et al. 2006, *Nature*, 444, 1044, doi: [10.1038/nature05376](https://doi.org/10.1038/nature05376)
- Ghirlanda, G., Ghisellini, G., Nava, L., & Burlon, D. 2011, *MNRAS*, 410, L47, doi: [10.1111/j.1745-3933.2010.00977.x](https://doi.org/10.1111/j.1745-3933.2010.00977.x)
- Goldstein, A., Veres, P., Burns, E., et al. 2017, *ApJL*, 848, L14, doi: [10.3847/2041-8213/aa8f41](https://doi.org/10.3847/2041-8213/aa8f41)
- Gottlieb, O., Issa, D., Jacquemin-Ide, J., et al. 2023a, *ApJL*, 954, L21, doi: [10.3847/2041-8213/aceeff](https://doi.org/10.3847/2041-8213/aceeff)
- Gottlieb, O., Metzger, B. D., Quataert, E., et al. 2023b, *ApJL*, 958, L33, doi: [10.3847/2041-8213/ad096e](https://doi.org/10.3847/2041-8213/ad096e)
- Hajela, A., Margutti, R., Bright, J. S., et al. 2022, *ApJL*, 927, L17, doi: [10.3847/2041-8213/ac504a](https://doi.org/10.3847/2041-8213/ac504a)
- Hallinan, G., Corsi, A., Mooley, K. P., et al. 2017, *Science*, 358, 1579, doi: [10.1126/science.aap9855](https://doi.org/10.1126/science.aap9855)
- Hamidani, H., Kimura, S. S., Tanaka, M., & Ioka, K. 2024, *ApJ*, 963, 137, doi: [10.3847/1538-4357/ad20d0](https://doi.org/10.3847/1538-4357/ad20d0)

- Janka, H. T., Eberl, T., Ruffert, M., & Fryer, C. L. 1999, *ApJL*, 527, L39, doi: [10.1086/312397](https://doi.org/10.1086/312397)
- Kasen, D., Badnell, N. R., & Barnes, J. 2013, *ApJ*, 774, 25, doi: [10.1088/0004-637X/774/1/25](https://doi.org/10.1088/0004-637X/774/1/25)
- Kawaguchi, K., Kyutoku, K., Nakano, H., et al. 2015, *PhRvD*, 92, 024014, doi: [10.1103/PhysRevD.92.024014](https://doi.org/10.1103/PhysRevD.92.024014)
- Kawaguchi, K., Kyutoku, K., Shibata, M., & Tanaka, M. 2016, *ApJ*, 825, 52, doi: [10.3847/0004-637X/825/1/52](https://doi.org/10.3847/0004-637X/825/1/52)
- Kisaka, S., & Ioka, K. 2015, *ApJL*, 804, L16, doi: [10.1088/2041-8205/804/1/L16](https://doi.org/10.1088/2041-8205/804/1/L16)
- Kouveliotou, C., Meegan, C. A., Fishman, G. J., et al. 1993, *ApJL*, 413, L101, doi: [10.1086/186969](https://doi.org/10.1086/186969)
- Kulkarni, S. R. 2005, arXiv e-prints, astro, doi: [10.48550/arXiv.astro-ph/0510256](https://doi.org/10.48550/arXiv.astro-ph/0510256)
- Lattimer, J. M. 2021, *Annual Review of Nuclear and Particle Science*, 71, 433, doi: [10.1146/annurev-nucl-102419-124827](https://doi.org/10.1146/annurev-nucl-102419-124827)
- Lazzati, D., & Perna, R. 2019, *ApJ*, 881, 89, doi: [10.3847/1538-4357/ab2e06](https://doi.org/10.3847/1538-4357/ab2e06)
- Levan, A. J., Gompertz, B. P., Salafia, O. S., et al. 2024, *Nature*, 626, 737, doi: [10.1038/s41586-023-06759-1](https://doi.org/10.1038/s41586-023-06759-1)
- Levesque, E. M., Bloom, J. S., Butler, N. R., et al. 2010, *MNRAS*, 401, 963, doi: [10.1111/j.1365-2966.2009.15733.x](https://doi.org/10.1111/j.1365-2966.2009.15733.x)
- Li, L.-X., & Paczyński, B. 1998, *ApJL*, 507, L59, doi: [10.1086/311680](https://doi.org/10.1086/311680)
- Liang, E.-W., Yi, S.-X., Zhang, J., et al. 2010, *ApJ*, 725, 2209, doi: [10.1088/0004-637X/725/2/2209](https://doi.org/10.1088/0004-637X/725/2/2209)
- Liu, T., Gu, W.-M., & Zhang, B. 2017, *NewAR*, 79, 1, doi: [10.1016/j.newar.2017.07.001](https://doi.org/10.1016/j.newar.2017.07.001)
- Lü, H.-J., Zhang, B., Lei, W.-H., Li, Y., & Lasky, P. D. 2015, *ApJ*, 805, 89, doi: [10.1088/0004-637X/805/2/89](https://doi.org/10.1088/0004-637X/805/2/89)
- Lu, W., & Quataert, E. 2023, *MNRAS*, 522, 5848, doi: [10.1093/mnras/stad1336](https://doi.org/10.1093/mnras/stad1336)
- Margalit, B., & Metzger, B. D. 2019, *ApJL*, 880, L15, doi: [10.3847/2041-8213/ab2ae2](https://doi.org/10.3847/2041-8213/ab2ae2)
- Mészáros, P., & Rees, M. J. 1997, *ApJ*, 476, 232, doi: [10.1086/303625](https://doi.org/10.1086/303625)
- . 1999, *MNRAS*, 306, L39, doi: [10.1046/j.1365-8711.1999.02800.x](https://doi.org/10.1046/j.1365-8711.1999.02800.x)
- Metzger, B. D., & Berger, E. 2012, *ApJ*, 746, 48, doi: [10.1088/0004-637X/746/1/48](https://doi.org/10.1088/0004-637X/746/1/48)
- Metzger, B. D., Quataert, E., & Thompson, T. A. 2008, *MNRAS*, 385, 1455, doi: [10.1111/j.1365-2966.2008.12923.x](https://doi.org/10.1111/j.1365-2966.2008.12923.x)
- Metzger, B. D., Martínez-Pinedo, G., Darbha, S., et al. 2010, *Monthly Notices of the Royal Astronomical Society*, 406, 2650, doi: [10.1111/j.1365-2966.2010.16864.x](https://doi.org/10.1111/j.1365-2966.2010.16864.x)
- Minaev, P. Y., & Pozanenko, A. S. 2020, *MNRAS*, 492, 1919, doi: [10.1093/mnras/stz3611](https://doi.org/10.1093/mnras/stz3611)
- Most, E. R., & Quataert, E. 2023, *ApJL*, 947, L15, doi: [10.3847/2041-8213/acca84](https://doi.org/10.3847/2041-8213/acca84)
- Norris, J. P., & Bonnell, J. T. 2006, *ApJ*, 643, 266, doi: [10.1086/502796](https://doi.org/10.1086/502796)
- Norris, J. P., Bonnell, J. T., Kazanas, D., et al. 2005, *ApJ*, 627, 324, doi: [10.1086/430294](https://doi.org/10.1086/430294)
- Perna, R., Armitage, P. J., & Zhang, B. 2006, *ApJL*, 636, L29, doi: [10.1086/499775](https://doi.org/10.1086/499775)
- Proga, D., & Zhang, B. 2006, *MNRAS*, 370, L61, doi: [10.1111/j.1745-3933.2006.00189.x](https://doi.org/10.1111/j.1745-3933.2006.00189.x)
- Quirola-Vásquez, J., Bauer, F. E., Jonker, P. G., et al. 2024, *A&A*, 683, A243, doi: [10.1051/0004-6361/202347629](https://doi.org/10.1051/0004-6361/202347629)
- Rastinejad, J. C., Gompertz, B. P., Levan, A. J., et al. 2022, *Nature*, 612, 223, doi: [10.1038/s41586-022-05390-w](https://doi.org/10.1038/s41586-022-05390-w)
- Rezzolla, L., Giacomazzo, B., Baiotti, L., et al. 2011, *ApJL*, 732, L6, doi: [10.1088/2041-8205/732/1/L6](https://doi.org/10.1088/2041-8205/732/1/L6)
- Rossi, A., Rothberg, B., Palazzi, E., et al. 2022, *ApJ*, 932, 1, doi: [10.3847/1538-4357/ac60a2](https://doi.org/10.3847/1538-4357/ac60a2)
- Rosswog, S., Ramirez-Ruiz, E., & Davies, M. B. 2003, *MNRAS*, 345, 1077, doi: [10.1046/j.1365-2966.2003.07032.x](https://doi.org/10.1046/j.1365-2966.2003.07032.x)
- Rowlinson, A., Gompertz, B. P., Dainotti, M., et al. 2014, *MNRAS*, 443, 1779, doi: [10.1093/mnras/stu1277](https://doi.org/10.1093/mnras/stu1277)
- Rowlinson, A., O'Brien, P. T., Metzger, B. D., Tanvir, N. R., & Levan, A. J. 2013, *MNRAS*, 430, 1061, doi: [10.1093/mnras/sts683](https://doi.org/10.1093/mnras/sts683)
- Rowlinson, A., O'Brien, P. T., Tanvir, N. R., et al. 2010, *MNRAS*, 409, 531, doi: [10.1111/j.1365-2966.2010.17354.x](https://doi.org/10.1111/j.1365-2966.2010.17354.x)
- Ruiz, M., Shapiro, S. L., & Tsokaros, A. 2018, *PhRvD*, 98, 123017, doi: [10.1103/PhysRevD.98.123017](https://doi.org/10.1103/PhysRevD.98.123017)
- . 2021, *Frontiers in Astronomy and Space Sciences*, 8, 39, doi: [10.3389/fspas.2021.656907](https://doi.org/10.3389/fspas.2021.656907)
- Sari, R., Piran, T., & Halpern, J. P. 1999, *ApJL*, 519, L17, doi: [10.1086/312109](https://doi.org/10.1086/312109)
- Sari, R., Piran, T., & Narayan, R. 1998, *ApJL*, 497, L17, doi: [10.1086/311269](https://doi.org/10.1086/311269)
- Savchenko, V., Ferrigno, C., Kuulkers, E., et al. 2017, *ApJL*, 848, L15, doi: [10.3847/2041-8213/aa8f94](https://doi.org/10.3847/2041-8213/aa8f94)
- Shapiro, S. L. 2000, *ApJ*, 544, 397, doi: [10.1086/317209](https://doi.org/10.1086/317209)
- Sun, H., Li, Y., Zhang, B.-B., et al. 2019, *ApJ*, 886, 129, doi: [10.3847/1538-4357/ab4bc7](https://doi.org/10.3847/1538-4357/ab4bc7)
- Sun, H., Zhang, B., & Gao, H. 2017, *ApJ*, 835, 7, doi: [10.3847/1538-4357/835/1/7](https://doi.org/10.3847/1538-4357/835/1/7)
- Sun, H., Wang, C. W., Yang, J., et al. 2025, *National Science Review*, 12, nwae401, doi: [10.1093/nsr/nwae401](https://doi.org/10.1093/nsr/nwae401)
- Troja, E., Piro, L., van Eerten, H., et al. 2017, *Nature*, 551, 71, doi: [10.1038/nature24290](https://doi.org/10.1038/nature24290)
- Troja, E., van Eerten, H., Ryan, G., et al. 2019a, *MNRAS*, 489, 1919, doi: [10.1093/mnras/stz2248](https://doi.org/10.1093/mnras/stz2248)
- . 2019b, *MNRAS*, 489, 1919, doi: [10.1093/mnras/stz2248](https://doi.org/10.1093/mnras/stz2248)

- Troja, E., van Eerten, H., Zhang, B., et al. 2020, MNRAS, 498, 5643, doi: [10.1093/mnras/staa2626](https://doi.org/10.1093/mnras/staa2626)
- Usov, V. V. 1992, Nature, 357, 472, doi: [10.1038/357472a0](https://doi.org/10.1038/357472a0)
- Valenti, S., Sand, D. J., Yang, S., et al. 2017, ApJL, 848, L24, doi: [10.3847/2041-8213/aa8edf](https://doi.org/10.3847/2041-8213/aa8edf)
- Villar, V. A., Guillochon, J., Berger, E., et al. 2017, ApJL, 851, L21, doi: [10.3847/2041-8213/aa9c84](https://doi.org/10.3847/2041-8213/aa9c84)
- Wang, Y., Zhang, B., & Zhu, Z. 2024, MNRAS, 528, 3705, doi: [10.1093/mnras/stae136](https://doi.org/10.1093/mnras/stae136)
- Wei, J., Cordier, B., Antier, S., et al. 2016, arXiv e-prints, arXiv:1610.06892, doi: [10.48550/arXiv.1610.06892](https://doi.org/10.48550/arXiv.1610.06892)
- Woosley, S. E., & Bloom, J. S. 2006, ARA&A, 44, 507, doi: [10.1146/annurev.astro.43.072103.150558](https://doi.org/10.1146/annurev.astro.43.072103.150558)
- Xiao, D., & Dai, Z.-G. 2019, ApJ, 878, 62, doi: [10.3847/1538-4357/ab12da](https://doi.org/10.3847/1538-4357/ab12da)
- Xin, L.-P., Liang, E.-W., Wei, J.-Y., et al. 2011, MNRAS, 410, 27, doi: [10.1111/j.1365-2966.2010.17419.x](https://doi.org/10.1111/j.1365-2966.2010.17419.x)
- Xue, Y. Q., Zheng, X. C., Li, Y., et al. 2019, Nature, 568, 198, doi: [10.1038/s41586-019-1079-5](https://doi.org/10.1038/s41586-019-1079-5)
- Yang, B., Jin, Z.-P., Li, X., et al. 2015, Nature Communications, 6, 7323, doi: [10.1038/ncomms8323](https://doi.org/10.1038/ncomms8323)
- Yang, J., Ai, S., Zhang, B.-B., et al. 2022, Nature, 612, 232, doi: [10.1038/s41586-022-05403-8](https://doi.org/10.1038/s41586-022-05403-8)
- Yang, Y.-H., Troja, E., O'Connor, B., et al. 2024, Nature, 626, 742, doi: [10.1038/s41586-023-06979-5](https://doi.org/10.1038/s41586-023-06979-5)
- Yu, Y.-W., Zhang, B., & Gao, H. 2013, ApJL, 776, L40, doi: [10.1088/2041-8205/776/2/L40](https://doi.org/10.1088/2041-8205/776/2/L40)
- Yuan, W., Zhang, C., Chen, Y., & Ling, Z. 2022, in Handbook of X-ray and Gamma-ray Astrophysics, ed. C. Bambi & A. Sanganelo, 86, doi: [10.1007/978-981-16-4544-0\\_151-1](https://doi.org/10.1007/978-981-16-4544-0_151-1)
- Zhang, B. 2006, Nature, 444, 1010, doi: [10.1038/4441010a](https://doi.org/10.1038/4441010a)
- . 2013, ApJL, 763, L22, doi: [10.1088/2041-8205/763/1/L22](https://doi.org/10.1088/2041-8205/763/1/L22)
- . 2018, The Physics of Gamma-Ray Bursts, doi: [10.1017/9781139226530](https://doi.org/10.1017/9781139226530)
- . 2025, Journal of High Energy Astrophysics, 45, 325, doi: [10.1016/j.jheap.2024.12.013](https://doi.org/10.1016/j.jheap.2024.12.013)
- Zhang, B., Kobayashi, S., & Mészáros, P. 2003, ApJ, 595, 950, doi: [10.1086/377363](https://doi.org/10.1086/377363)
- Zhang, B., & Mészáros, P. 2001, ApJL, 552, L35, doi: [10.1086/320255](https://doi.org/10.1086/320255)
- . 2002, ApJ, 571, 876, doi: [10.1086/339981](https://doi.org/10.1086/339981)
- Zhang, B., Zhang, B.-B., Liang, E.-W., et al. 2007, ApJL, 655, L25, doi: [10.1086/511781](https://doi.org/10.1086/511781)
- Zhang, B., Zhang, B.-B., Virgili, F. J., et al. 2009, ApJ, 703, 1696, doi: [10.1088/0004-637X/703/2/1696](https://doi.org/10.1088/0004-637X/703/2/1696)
- Zhang, B. B., Zhang, B., Sun, H., et al. 2018a, Nature Communications, 9, 447, doi: [10.1038/s41467-018-02847-3](https://doi.org/10.1038/s41467-018-02847-3)
- . 2018b, Nature Communications, 9, 447, doi: [10.1038/s41467-018-02847-3](https://doi.org/10.1038/s41467-018-02847-3)
- Zhu, J.-P., Wang, X. I., Sun, H., et al. 2022, ApJL, 936, L10, doi: [10.3847/2041-8213/ac85ad](https://doi.org/10.3847/2041-8213/ac85ad)